O.V. Lounasmaa Laboratory

Novel diffusion tensor imaging (DTI) approaches at 3 T

Jaana Hiltunen

Aalto University

DOCTORAL DISSERTATIONS

Aalto University publication series
DOCTORAL DISSERTATIONS 93/2013

Novel diffusion tensor imaging (DTI) approaches at 3 T

Jaana Hiltunen

A doctoral dissertation completed for the degree of Doctor of Philosophy to be defended, with the permission of the Aalto University School of Science, at a public examination held at the Auditorium TU1 at the Aalto University on 30th of May 2013 at 12.

Aalto University
School of Science
O.V. Lounasmaa Laboratory
Brain Research Unit

Supervising professors
Acad. Prof. Riitta Hari
Brain Research Unit
O.V. Lounasmaa Laboratory
School of Science
Aalto University
Finland

Thesis advisors
Acad. Prof. Riitta Hari
Brain Research Unit
O.V. Lounasmaa Laboratory
School of Science
Aalto University
Finland

Preliminary examiners
Prof. Andrew Alexander
Waisman Laboratory for Brain Imaging and Behavior
University of Wisconsin
USA

Prof. Hannu Eskola
Department of Electronics and Communications Engineering
Tampere University of Technology
Finland

Opponents
Dr. Carlo Pierpaoli
National Institute of Child Health and Human Development (NICHD)
National Institute of Health (NIH)
USA

Aalto University publication series
DOCTORAL DISSERTATIONS 93/2013

ISBN 978-952-60-5196-3 (printed)
ISBN 978-952-60-5197-0 (pdf)
ISSN-L 1799-4934
ISSN 1799-4934 (printed)
ISSN 1799-4942 (pdf)
http://urn.fi/URN:ISBN:978-952-60-5197-0

Unigrafia Oy
Helsinki 2013

Finland

441 697
Printed matter

Aalto University

Abstract

Aalto University, P.O. Box 11000, FI-00076 Aalto www.aalto.fi

Author
Jaana Hiltunen

Name of the doctoral dissertation
Novel diffusion tensor imaging (DTI) approaches at 3 T

Publisher School of Science

Unit O.V. Lounasmaa Laboratory

Series Aalto University publication series DOCTORAL DISSERTATIONS 93/2013

Field of research Biomedical Engineering and Biophysics

Manuscript submitted 13 March 2013 **Date of the defence** 30 May 2013

Permission to publish granted (date) 6 May 2013 **Language** English

☐ **Monograph** ☒ **Article dissertation (summary + original articles)**

Abstract

Diffusion tensor imaging (DTI) records random thermal movements of water molecules in the body. In tissues with organized microstructure, such as the white matter of the brain, water tends to move (diffuse) more easily along the main direction of the fibers than in the orthogonal directions, resulting in anisotropic diffusion. The main parameter images of interest are the mean diffusivity (MD) describing the strength of diffusion, fractional anisotropy (FA) describing the asymmetry of diffusion (due to tissue structures), and tractography to visualize the 3D course of fiber tracts.

This Thesis arose from the methodological needs related to adoption of the DTI method into our laboratory. In the first study, mechanical vibrations during DTI were demonstrated to be unevenly distributed within the scanner. These vibrations, generally assumed to be negligible, thus have to be taken into consideration, as they may affect the image quality and accuracy of diffusion measurements. In the second study, pre-processing-effects of voxel-based analysis (VBA) of DTI data were evaluated using simulated brain lesions in MD and FA images. Pre-processing and inter-individual variation remarkably affected the outcome of the analysis even to such extent that some lesions were not detected by VBA. The success of lesion detection varied between the brain areas, and it was different for MD and FA. The third study was the first to demonstrate the feasibility of DTI in tracking distal peripheral nerves in both upper and lower limbs. As a continuation, DTI was in the fourth study applied to monitor patients with carpal tunnel syndrome, an entrapment of the median nerve at the wrist, before and after surgical therapy. Comparisons with healthy young control subjects revealed increased MD and decreased FA in patients, whereas results of patients and age-matched control subjects were rather similar. Post-operative healing was reflected in MD but not in FA. Numerous other DTI studies on peripheral nerves, published recently, indicate that this research area initiated by us is becoming increasingly popular.

Keywords diffusion tensor imaging, DTI, vibration, voxel-based analysis, peripheral nerves, carpal tunnel syndrome

ISBN (printed) 978-952-60-5196-3 **ISBN (pdf)** 978-952-60-5197-0

ISSN-L 1799-4934 **ISSN (printed)** 1799-4934 **ISSN (pdf)** 1799-4942

Location of publisher Espoo **Location of printing** Helsinki **Year** 2013

Pages 79 **urn** http://urn.fi/URN:ISBN:978-952-60-5197-0

A? Aalto-yliopisto

Tiivistelmä

Aalto-yliopisto, PL 11000, 00076 Aalto www.aalto.fi

Tekijä
Jaana Hiltunen

Väitöskirjan nimi
Uusia näkökulmia 3 teslan diffuusiotensorikuvaukseen (DTI)

Julkaisija Perustieteiden korkeakoulu

Yksikkö O.V. Lounasmaa -laboratorio

Sarja Aalto University publication series DOCTORAL DISSERTATIONS 93/2013

Tutkimusala Lääketieteellinen tekniikka ja biofysiikka

Käsikirjoituksen pvm 13.03.2013 **Väitöspäivä** 30.05.2013

Julkaisuluvan myöntämispäivä 06.05.2013 **Kieli** Englanti

☐ **Monografia** ☒ **Yhdistelmäväitöskirja (yhteenveto-osa + erillisartikkelit)**

Tiivistelmä

Diffuusiotensorikuvauksella (DTI) mitataan vesimolekyylien lämpöliikettä kehossa ihmiseen kajoamatta. Järjestyneissä kudosrakenteissa (esimerkiksi aivojen valkeassa aineessa) on säikeitä, joiden suunnassa vesi diffundoituu paremmin kuin kohtisuoraan säikeitä vastaan; seurauksena on diffuusion anisotropia eli epäsymmetria. Kuva-analyyseissä mielenkiinnon kohteina ovat yleensä keskimääräinen diffuusion suuruus, kudosrakenteiden aikaansaama anisotropia ja traktografia eli hermoratojen kartoitus, jolla hermoratoja voidaan visualisoida kolmiulotteisesti.

Tämän väitöskirjan liipaisijana olivat uudet menetelmälliset haasteet, jotka liittyivät DTI-menetelmän käyttöönottoon laboratoriossamme. Ensimmäisessä osatyössä osoitettiin DTI-kuvauksen synnyttämän mekaanisen tärinän leviävän epätasaisesti kuvauslaitteen rakenteissa. Tämän vuoksi tärinän mahdollinen vaikutus kuvanlaatuun ja diffuusiomittausten tarkkuuteen on syytä huomioida, vaikka tärinän on aiemmin yleisesti arveltu olevan merkityksetöntä. Toisessa osatyössä tutkittiin kuvien esikäsittelyn vaikutusta vokselipohjaisen analyysin (VBA) tuloksiin käyttäen oikeita vaurioita jäljitteleviä keinotekoisia muutoksia MD- ja FA-kuvissa. Esikäsittely ja koehenkilöiden väliset eroavuudet vaikuttivat analyysien tuloksiin jopa niin suuressa määrin, että osa vauriokohdista jäi kokonaan löytymättä. Esikäsittelyn vaikutukset olivat erilaisia eri aivoalueilla ja myös MD- ja FA-kuvissa. Kolmannessa osatyössä osoitettiin ensimmäistä kertaa DTI:n soveltuvan ylä- ja alaraajojen distaalisten ääreishermojen kuvaukseen. Neljännessä osatyössä diffuusiotensorikuvauksella tutkittiin potilaita, joilla on todettu karpaalitunnelisyndrooma (yläraajan keskihermon pinnetila ranteessa) sekä ennen että jälkeen leikkaushoidon. Verrattuna nuorten verrokkihenkilöiden tuloksiin, potilaiden keskihermossa diffuusio oli lisääntynyt ja anisotropia vähentynyt, kun taas potilaiden ja samaan ikäluokkaan kuuluvien verrokkien tulokset olivat varsin samankaltaisia. Leikkauksen jälkeinen paraneminen näkyi diffuusion suuruudessa, mutta ei anisotropiassa. Myös ikä näytti vaikuttavan diffuusio- ja anisotropiatuloksiin. Viime aikoina on julkaistu lukuisa määrä ääreishermojen diffuusiotensorikuvaustutkimuksia ja vaikuttaa siltä, että tämän käynnistämämme tutkimusalueen suosio on nopeasti kasvamassa.

Avainsanat diffuusiotensorikuvaus, DTI, tärinä, vokselipohjainen analyysi, ääreishermot, karpaalitunnelisyndrooma

ISBN (painettu) 978-952-60-5196-3 **ISBN (pdf)** 978-952-60-5197-0

ISSN-L 1799-4934 **ISSN (painettu)** 1799-4934 **ISSN (pdf)** 1799-4942

Julkaisupaikka Espoo **Painopaikka** Helsinki **Vuosi** 2013

Sivumäärä 79 **urn** http://urn.fi/URN:ISBN:978-952-60-5197-0

Table of contents

List of publications

This thesis consists of the summary and four original publications:

P1. **Hiltunen J**, Hari R, Jousmäki V, Müller K, Sepponen R, and Joensuu R: Quantification of mechanical vibration during diffusion tensor imaging at 3 T. NeuroImage 2006, 32: 93–103.

P2. **Hiltunen J**, Seppä M, and Hari R: Evaluation of voxel-based group-level analysis of diffusion tensor images using simulated brain lesions. Neuroscience Research 2011, 71: 377–386.

P3. **Hiltunen J**, Suortti T, Arvela S, Seppä M, Joensuu R, and Hari R: Diffusion tensor imaging and tractography of distal peripheral nerves at 3 T. Clinical Neurophysiology 2005, 116: 2315–2323.

P4. **Hiltunen J**, Kirveskari E, Numminen J, Lindfors N, Göransson H, and Hari R: Pre- and post-operative diffusion tensor imaging of median nerve in carpal tunnel syndrome. European Radiology 2012, 22:1310–1319.

Contribution of the author

As the first author of all publications, I had the main responsibility to analyse the data and write the publications, with active participation of the co-authors. In P1, I also actively participated in the planning of the study, recorded all vibration data together with a co-author, analysed the data, and visualized the results, partially with self-made Matlab scripts. In P2, I had a major role in the planning of the study, I recorded all the imaging data and analysed the simulated data, partially with self-made Matlab scripts. In P3, I actively participated in the planning of study, and I recorded and analysed the imaging data with the help of a co-author. In P4, I planned the study with input from co-authors, recorded part of the data, and analysed all the data (excluding clinical and radiological evaluations).

Abbreviations

ADC	apparent diffusion coefficient
BET	brain extraction tool
CC	corpus callosum
CHARMED	composite hindered and restricted model for diffusion
CSF	cerebrospinal fluid
CST	cortico-spinal tract
CTS	carpal tunnel syndrome
DEC	direction-encoded color (map)
DKI	diffusion kurtosis imaging
DSI	diffusion spectrum imaging
DTI	diffusion tensor imaging
DWI	diffusion-weighted imaging/images
ECC	eddy current compensation
EPI	echo planar imaging
FA	fractional anisotropy
FACT	fiber assigning by continuous tracking
FID	free induction decay
FOV	field of view
FSE	fast spin-echo
FWE	family-wise error (rate correction)
FWHM	full-width at half maximum
HARDI	high angular resolution diffusion imaging
MD	mean diffusivity
MNI	Montreal Neurological Institute
MR	magnetic resonance
MRI	magnetic resonance imaging/images
NMR	nuclear magnetic resonance
PASMRI	persistent angular structure magnetic resonance imaging
PDF	probability density function
QSI	Q-space imaging
RF	radio-frequency
ROI	region of interest
SE	spin echo
SLF	superior longitudinal fasciculus
SNR	signal-to-noise ratio
SPGR	spoiled gradient echo
SPM	statistical parametric mapping/maps
SS	single shot
STIR	short-tau inversion recovery
TE	echo time
TBSS	tract-based spatial statistics
TR	repetition time
VBA	voxel-based analysis

1 Introduction

Diffusion tensor imaging (DTI), a technique based on magnetic resonance imaging (MRI), can reveal tissue microstructure noninvasively by monitoring random movements of water molecules in tissues (Basser et al. 1994b, Le Bihan 1995, Le Bihan et al. 2001). DTI is an especially advantageous imaging method in tissues with organized microstructure, such as the white matter of the brain. Such tissues comprise fiber bundles along which the water molecules tend to move more easily than in the orthogonal directions, resulting in anisotropy (inhomogeneity of diffusion). The measured diffusion-weighted images are typically further analyzed to obtain parameter images (maps) that describe different characteristics of diffusion. For example, mean diffusivity (MD) is an absolute measure of the strength of diffusion, whereas fractional anisotropy (FA) describes the asymmetry of diffusion due to tissue structures. Moreover, tractography can be used to visualize the 3D course of fiber tracts. Before DTI, this kind of information about tissue structures was available only *post-mortem*.

DTI was introduced in 1994 by Basser and coworkers (1994b) with ex-vivo animal samples as test objects. This innovation was, however, already preceded by diffusion recordings and quantitative apparent diffusion coefficient (ADC) maps by means of nuclear magnetic resonance (NMR) spectroscopy (Le Bihan et al. 1986); the first ADC applications were in brain research (Le Bihan et al. 1986, Moseley et al. 1990). The main DTI applications have remained in basic brain research and in studies of white matter connectivity in the human brain, although clinical applications are emerging as well. Today, DTI is being used for imaging various anatomical structures and organs, such as peripheral nerves, spine, muscles, and kidneys, mainly with small sample sizes to show the feasibility of the method. The main clinical applications of DTI are in neurology, especially in the differential diagnostics of stroke patients by means of ADC and MD, and in studies of various disorders involving white matter. Moreover, the number of MD recordings of structures and organs in the body has recently grown tremendously, and recording the direction of diffusion by means of FA could be advantageous and provide useful information about tissue structures and pathologies.

Although DTI has drawbacks, such as limited resolution and image distortions due to echo planar imaging (EPI) acquisition, its clear strengths are its

quantitative and non-invasive nature without the need for contrast agents or ionizing radiation.

Publications P1 and P2 emerged from methodological development work necessary for adopting the DTI method into our laboratory, whereas publications P3 and P4 introduce novel applications for DTI. In P1, we quantified mechanical vibrations during DTI with various imaging parameters using a laser-based interferometer. These vibrations have generally been assumed to be negligible. In P2, we evaluated the performance of voxel-based analysis (VBA) using simulated brain lesions in MD and FA images. We applied conventional VBA to DTI images, ignoring the most recent innovations and improvements to follow mainstream DTI–VBA applications at that time. In P3, we suggested DTI, as a quantitative and more objective analysis method than only the visual inspection of MR images, for studies of distal peripheral nerves. As a continuation, in P4, we monitored, by means of DTI (and MRI), median-nerve integrity in patients with carpal tunnel syndrome before and after surgical therapy. We also studied age effects in healthy subjects, and we introduced a novel slice-wise analysis for patient diagnostics.

This summary first provides the basics of DTI and then briefly summarizes the methods and results of Publications P1–P4 that are appended to this thesis. Chapter 2 presents the basics of MRI, the concept of diffusion, and the methodological core of the thesis, that is, the measurements, image analysis, and main DTI applications. Chapter 3 provides the objectives of this thesis. Chapter 4 summarizes the background, motivation, methods, main results and brief conclusions of publications P1–P4. Finally, Chapter 5 summarizes and integrates the findings, providing a general discussion for all results of this thesis.

2 Background

2.1 Magnetic Resonance Imaging (MRI)

In this Section, the basics of MRI physics are discussed to the extent required for understanding the rationale and results of the present thesis. The text is based on the books of Liang and Lauterburg (2000), Bernstein and co-authors (2004), Westbrook and co-authors (2005), and McRobbie and co-authors (2007).

2.1.1 Nuclear magnetic resonance (NMR)

Nuclei with unpaired protons, neutrons, or both, have a non-zero angular momentum J and can therefore produce NMR signal that is measurable by means of magnetic resonance imaging. Since approximately 2/3 of human tissues are water, hydrogen nuclei ^{1}H are most commonly used in MRI.

These nuclei with angular momentum J, often referred to as spins, possess a magnetic moment μ

$$\mu = \gamma J, \tag{1}$$

where γ is the nucleus-specific gyromagnetic ratio; for the hydrogen nucleus, $\gamma/2\pi$ = 42.6 MHz/T. The magnitude of μ (with and without external magnetic field) is

$$\mu = \gamma\hbar\sqrt{I(I+1)}, \tag{2}$$

where $\hbar = \mathrm{h}/2\pi$, h is Planck's constant, and $I = 1/2$ is nuclear spin quantum number for ^{1}H.

In the absence of an external magnetic field, the magnetic moments are oriented randomly. However, when spins are placed in an external magnetic field B_0, magnetic moments μ take one of the two possible orientations (in ^{1}H parallel or antiparallel), and they start to precess, see Figure 1.

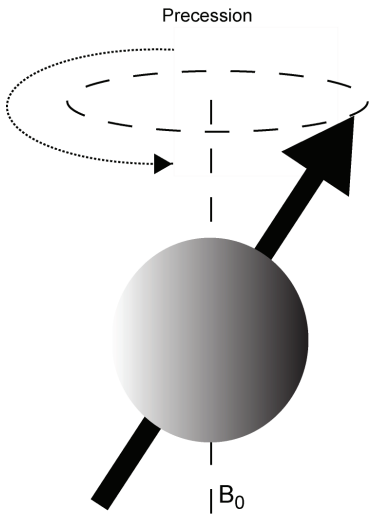

Figure 1: Precession causes the magnetic moment (*black arrow*) of nucleus (*gray sphere)* to follow a circular path (*dashed line*) around main magnetic field B_0 at precession frequency ω_0.

The angular frequency of precession ω_0, also called the Larmor frequency, depends on the external magnetic field B_0

$$\omega_0 = 2\pi f = \gamma B_0. \tag{3}$$

At 3 T, the hydrogen nuclei thus precess at f = 127.7 MHz.

The Zeeman effect splits the magnetic moments μ in B_0 into nuclear energy levels

$$E = -\mu B_0 = -m\,\gamma\,\hbar B_0, \tag{4}$$

where $m = \pm I = \pm 1/2$ for ^{1}H. Protons can thus have two energy states, one parallel and the other antiparallel to the main magnetic field. The parallel state has lower energy and is more stable; therefore, the lower energy state is slightly more populated: an excess of approximately 2 protons out of 10^5 water molecules at 3 T are in the parallel *vs*. the antiparallel (higher energy, or excited) state. The relative proportion of these two spin states depends on their energy difference ΔE, absolute temperature T, and the Boltzmann's constant k

$$N_{\text{parallel}}/N_{\text{antiparallel}} = e^{(\Delta E/kT)}. \tag{5}$$

A change from the low-energy to high-energy state is accomplished by means of resonance, which is obtained by exposing the spins to energy in packets of

$$\Delta E = \gamma \hbar B_0 = \hbar \omega_0, \tag{6}$$

transmitted at the Larmor (resonance) frequency ω_0.

The MRI signal is proportional to the net magnetization of all spins in the imaging volume. The net magnetization M_0 (at equilibrium) depends on the difference between the number of spins in the parallel and antiparallel states, and it increases as a function of field strength B_0.

2.1.2 Image acquisition

2.1.2.1 Excitation and relaxation

During MRI, the patient is positioned in the main magnetic field B_0 of the MRI scanner, aligned typically in the *z*-direction (by assumption, the direction of B_0). The anatomical area of interest is selected and divided into slices, which are then subjected to the radio-frequency (RF) magnetic field B_1, applied in short pulses at the Larmor frequency ω_0. These RF pulses excite the protons of water molecules, typically in one slice at a time, and tilt the net magnetization M_0 with respect to the main magnetic field B_0 towards orthogonal *xy*-plane. The commonly applied 90° pulse tilts M_0 by 90° into the *xy*-plane. Immediately after excitation, the individual magnetic moments are in phase and begin precessing about B_0, thereby producing a transverse magnetization M_{xy}, the basis of the MR signal. As the spins precess, they also start to dephase (lose phase coherence) and the spin system returns to thermal equilibrium; this return is characterized by transverse and longitudinal relaxations.

Figure 2 (left panel) shows that during transverse relaxation, the precessing magnetization decays exponentially with a time constant *T2*. This T2 relaxation, often referred to as spin–spin relaxation, is due to spin–spin interactions that lead to dephasing of spins, and thereby signal decay. Moreover, extrinsic sources of dephasing, such as magnetic field inhomogenities, cause slight variations in local field strengths, thus affecting the precession frequencies of spins. The signal decay that reflects both the spin–spin interactions and field inhomogeneities is called T2* decay, utilized in functional MRI.

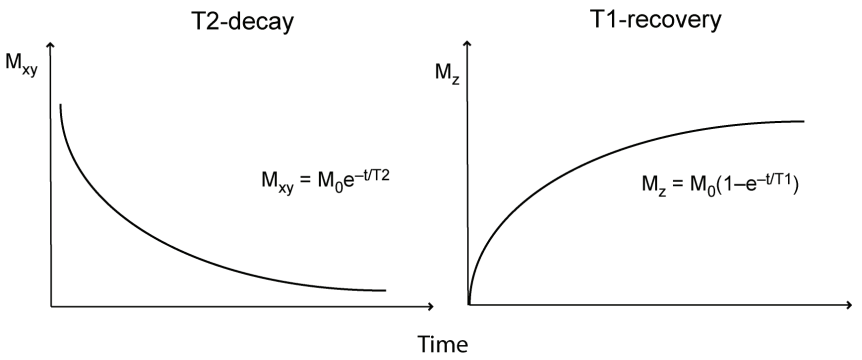

Figure 2: T2-relaxation describes the decay of transverse magnetization M_{xy} as a function of time (*left panel*), whereas T1-relaxation describes the recovery of longitudinal magnetization M_z as a function of time (*right panel*).

Simultaneously with T2 relaxation, the net magnetization starts to realign along the direction of B_0 with a relaxation time *T1*, as is shown in Figure 2 (right panel). Longitudinal relaxation T1, often referred to as spin–lattice relaxation, is due to energy exchange between spins and lattice.

During relaxation, spins in the imaging volume transmit a decreasing signal (FID, free induction decay) that can be recorded with a receiver coil. Typically this immediate signal decay is not recorded but instead, another RF pulse is applied at time τ after the excitation to eliminate the spin dephasing. In the spin echo (SE) pulse sequence, this RF pulse refocuses the spins so that they will be maximally in phase at time 2τ after the initial excitation, producing an echo that can be recorded.

Relaxation times vary in different tissues, resulting in different contrasts in the MR images. Moreover, image contrast can be adjusted by selection of the pulse sequence and imaging parameters, mainly with repetition time (TR) and echo time (TE).

2.1.2.2 Slice selection, spatial encoding and image formation

The spatial origin of the MR signal is encoded by means of gradient magnetic fields in the *x*-, *y*-, and *z*-directions. The gradients cause a linear change in the magnetic field along these three orthogonal directions. The scanned anatomical area, such as the whole brain, consists of a stack of 2D slices with a certain thickness (3D pulse sequences are beyond this thesis). Figure 3 demonstrates slice selection: each slice is selected by applying a magnetic field gradient perpendicular to the slice direction, and by applying an RF field at the Larmor frequency band (centre frequency ± offset frequency) of spins within the slice.

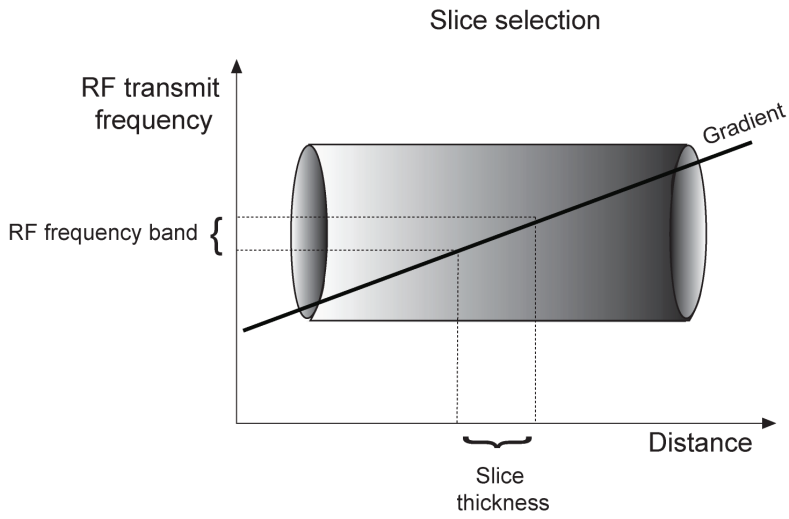

Figure 3: Magnetic field gradient together with RF magnetic field at Larmor frequency band excites spins only within a certain slice. The frequency band defines the location of the slice, whereas the gradient slope determines slice thickness. The slice location along the gradient (*i.e.* different slice) can be changed by shifting the frequency band of the RF pulse.

After spin excitation during slice selection, gradients along the two within-slice directions (x, y) are applied. Phase encoding gradient $G_y(t)$ changes the magnetic field along y-direction resulting in spatial variations in the precession frequency $\omega(y,t) = \omega_0 + \gamma\, G_y(t)y$. When the gradient is turned off, the precession frequency becomes equal along the y-axis, but the phase difference $\phi(y)$, accumulated during phase encoding time T_{pe}

$$\phi(y) = \gamma G_y y T_{pe} \tag{7}$$

remains and the signal is thus phase encoded. Similarly, frequency encoding gradient $G_x(t)$ during the readout causes spatial variations in the precession frequency

$$\omega(x,t) = \omega_0 + \gamma\, G_x(t)x, \tag{8}$$

which is thus linearly related to the spatial location of excited spins. During a typical pulse sequence, a slice is first selected, then phase information within the

slice is encoded (with one gradient amplitude at a time), and the imaging data is sampled with constant frequency encoding gradient on. Different amplitudes of phase encoding gradients are applied to obtain a unique phase for each spatial location.

The signal $S(k_x, k_y)$, recorded by a receiver coil and organized in the k-space, can be expressed as

$$S(k_x, k_y) = \iint f(x,y) e^{-i2\pi(k_x x + k_y y)} dx dy, \tag{9}$$

where

$$k_x(t) = \gamma \int G_x(t) dt \text{ and}$$
$$k_y(t) = \gamma \int G_y(t) dt \tag{10}$$

are integrals over the gradient lobes G_x and G_y, and $f(x,y)$ is the gray scale MR image, obtained as an inverse 2D Fourier transform of the k-space signal $S(k_x, k_y)$. The horizontal (k_x) axis represents frequency information and the vertical axis (k_y) the phase information, as is illustrated in Figure 4.

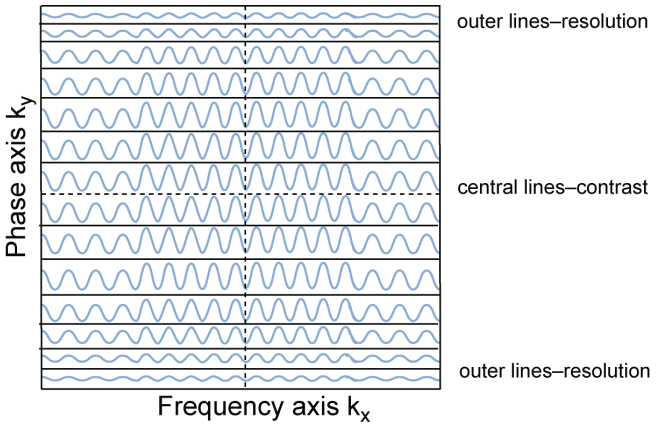

Figure 4: Schematic illustration of k-space data for a single slice. Each line is recorded with a different phase-encoding gradient amplitude. The outer lines are recorded with steep gradient amplitudes resulting in large dephasing and thereby low signal amplitudes, whereas central lines are recorded with gradual gradient amplitudes resulting in high signal, respectively.

The amplitude of frequency and phase encoding gradients determine the size of field of view (FOV) in the corresponding directions, whereas image matrix size is defined by the number of phase encoding steps, and by the number of data points recorded during the readout period (frequency encoding direction). The center of k-space, recorded with gradual phase encoding gradient amplitudes, determines the contrast of an image, whereas outer lines, recorded with steep gradient amplitudes, determine spatial information and resolution.

2.1.2.3 Signal-to-noise ratio (SNR) in MRI

Noise in MRI can arise from the subject, receiver coil, and electronics of the MRI system. At higher field strengths, such as 3 T applied in this thesis, the noise from subject dominates. Noise originates from random motion of electrons within conducting electrical parts and human tissues, and as it is random in nature (both spatially and temporally), it appears at all frequencies. Noise in the reconstructed images is distributed uniformly throughout the image and it makes the image look grainy.

The MRI signal is practically a voltage recorded using receiver coil after the RF excitation when net magnetization precesses in the transverse plane. When an image has been reconstructed, signal appears as the voxel intensity value (brightness). We cannot control the random noise, but we can affect the signal level. Larger signals can be obtained at stronger main magnetic field, in anatomical areas with higher proton density, and with larger voxel volumes, as well as with proper selection of the imaging parameters (TR, TE, flip angle, number of excitations/averages, receiver bandwidth) and of the receiver coil. In practice, the easiest way to affect the signal is to adjust the voxel size. As large voxels contain more spins to contribute to the signal, any parameter that increases the voxel size (FOV, matrix size, slice thickness) improves the SNR. Moreover, the receiver coil has an important role. Most of the present coils are multichannel phased array (surface) coils that add together signals from several coil elements and are positioned close to the area to be imaged, thereby optimally recording the signal.

Mathematically, $\mathrm{SNR} = \mathrm{S}/\sigma$, where S is the signal intensity in the tissue and σ is the standard deviation of the background (voxels out of tissue); the values for signal and background noise are obtained using a region-of-interest (ROI) analysis. However, in practice, SNR measurement protocol carried out for quality assurance may be slightly different, depending on coils, sequences, and scanners.

2.2 Diffusion

2.2.1 Thermal diffusion

Constant random microscopic motion of water molecules due to thermal energy is referred to as thermal diffusion, Brownian motion, or random thermal motion. According to Einstein's equation, the *n*-dimensional approximation for displacement x of water molecules at constant temperature is

$$x = \sqrt{2nDT_d}, \tag{11}$$

where n = 1, 2, 3 is the dimension of measurement, D is the diffusion coefficient, and T_d is the diffusion time. The diffusion coefficient is sensitive to temperature so that a 1 °C change in temperature corresponds to a 2.4% change in diffusion coefficient (Le Bihan et al. 1989). For free water molecules (in water) at 37°C, the diffusion coefficient is approximately 3 x 10^{-3} mm^2/s. In a free medium, the displacement of water molecules follows the 3-dimensional Gaussian distribution.

2.2.2 Diffusion in tissues

The diffusion coefficient D is valid only for homogeneous fluid with free diffusion. For example, in neural tissue, several factors affect the diffusion coefficient, such as the cell membrane and its permeability, transport mechanisms, and macromolecules. In such case, diffusion can be hindered or restricted, and result in decreased diffusion coefficient when diffusion time is increased (Hansen 1971, Cooper et al. 1974). Therefore, the term apparent diffusion coefficient (ADC) (Le Bihan et al. 1986, Le Bihan 1991) or diffusivity (Basser and Pierpaoli 1996) has been used to describe the strength of diffusion in biological tissues.

Water in the human body is thus constantly moving due to thermal energy (diffusion), but the movement is restricted and often has a preferred direction as the water molecules collide with other molecules and cell structures and move through membranes (Le Bihan 2003). Diffusion is homogeneous in all directions (isotropic) in free space and in tissues with random microstructure. However, in tissues with ordered microstructure such as tight fiber bundles in the white matter of the brain, the water diffuses more along the nerve fibers than transverse to them, and thus the diffusion is anisotropic rather than isotropic (Moseley et al. 1990).

Several reasons for anisotropy have been suggested, such as myelin, axonal membranes, neurofibrils, fast axonal transport, and susceptibility (see Beaulieu (2002, 2009) for reviews). However, a general view emerging from both animal and human studies suggests that anisotropic diffusion in neural fibers is due to tightly-packed axons and axonal membranes that cause a preferential direction for diffusion along the fibers and hinder diffusion perpendicular to fibers (Beaulieu 2009). Myelin is not the primary reason for anisotropy, although it may modulate the degree of anisotropy.

2.3 Diffusion MRI

2.3.1 Diffusion-weighted MRI

Diffusion-weighted imaging (DWI) provides an image contrast that depends on the diffusion of water molecules within tissues. Clinically, DWI is especially advantageous in the early detection of acute cerebral ischemia (Weber et al. 2000) and in studying the dynamics and phase (acute, subacute, or chronic) of ischemic stroke (Moseley et al. 1995, Weber et al. 2000). Moreover, DWI has also been applied to predict clinical outcome and improvement after the ischemic stroke (Warach et al. 1996, Van Everdingen et al. 1998), and to predict the risk of intracranial cerebral hemorrhage, a dangerous complication of thrombolytic therapy (Tong et al. 2000, Selim et al. 2002).

However, due to limitations in the clinical DWI pulse sequences (the diffusion can be measured only along the three gradient axes, one axis at the time), only the *strength* of diffusion can be defined by means of ADC or MD. To obtain information about the *direction* of diffusion, at least six diffusion gradient directions have to be measured with a specific DTI sequence.

2.3.2 Diffusion tensor imaging (DTI)

In diffusion tensor imaging, the measurement is sensitized to diffusion in one predetermined direction at a time by using magnetic gradients (Stejskal and Tanner 1965). The measurement is repeated several times, each in different directions ($\geq$ 6), and once without diffusion gradients to produce a reference image (b_0-image) required for quantification of diffusion. The directions are selected by applying

diffusion sensitizing gradients along the *x*-, *y*-, or *z*-axis. In contrast to DWI, any combination of these axes can be selected to measure oblique planes.

The most commonly used sequence in DTI recordings is an SE single-shot (SS) EPI sequence. The sequence is made diffusion-sensitive by applying a dephasing followed by a rephasing diffusion-sensitizing gradient positioned symmetrically with respect to a 180° RF refocusing pulse (Stejskal and Tanner 1965), see Figure 5.

Both these gradients cause an equal phase difference between the spins. The refocusing pulse applied in between the two gradients reverses the phase difference caused by the first gradient. If water molecules/spins remain stationary between the gradients, the total phase difference cancels out (complete refocusing). However, with diffusing spins, the total phase difference is non-zero, resulting in a signal loss (incomplete refocusing) that can be measured with MRI equipment.

DTI typically applies an EPI technique that allows the imaging data for one slice to be collected with a single RF excitation, an oscillating readout gradient, and a blipped phase-encoding gradient (Figure 5).

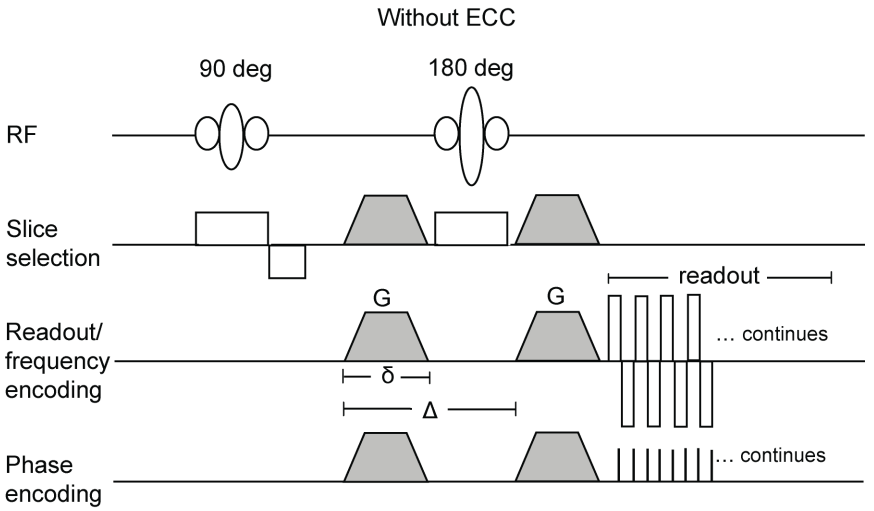

Figure 5: A schematic diagram of SE-SS-EPI (spin-echo single-shot echo planar imaging) sequence applied in the DTI studies. The diffusion-sensitizing gradients, shown as gray, are controlled by means of G = gradient amplitude, Δ= time between successive diffusion-sensitizing gradients, δ = duration of the diffusion-sensitizing gradient to obtain the desired diffusion-weighting in the images. Figure from P1.

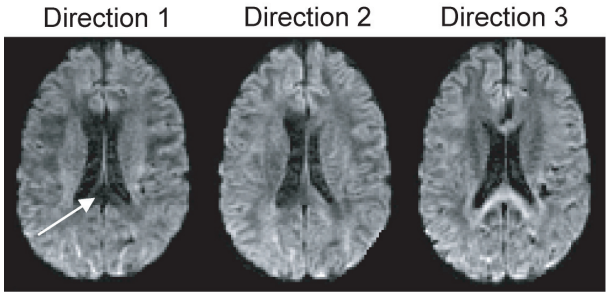

Figure 6: An example of diffusion-weighted brain images. Measurement of each slice is sensitive to diffusion in one direction only. Strong diffusion (direction 1) in the splenium of the corpus callosum (*white arrow*) and in the ventricles (all directions) appears as dark in the images. Figure from Hiltunen et al. (2007) with the courtesy of Duodecim.

2.3.2.1 Diffusion-weighting

Each diffusion measurement in a certain direction produces an image that characterizes diffusion in that direction. Diffusion in the direction of the diffusion-sensitizing gradient attenuates the measured MRI signal and is dark in the diffusion-weighted images. Figure 6 shows an example of a diffusion-weighted axial brain slice with different diffusion-sensitizing gradient orientations. The diffusion is strong in the right–left direction in the splenium of the corpus callosum (Figure 6, left panel) which thus appears as dark (area marked with an arrow in the image).

The signal intensity S_i along direction i (i = 1, …, N; N ≥ 6) in diffusion-weighted images is (Le Bihan 1991)

$$S_i = S_0 \exp(-b_i \, \mathrm{ADC}_i) = S_0 \exp(-b_i \, g_i \boldsymbol{D} g_i), \tag{12}$$

where S_i and S_0 are the signal intensities with and without diffusion weighting, ADC_i is the apparent diffusion coefficient along direction i (*i.e.* projection of $\boldsymbol{D}$ along g_i), b_i (s/mm^2) defines diffusion weighting in the images, $\boldsymbol{D}$ (mm^2/s) is the diffusion tensor, and g_i is a unit vector containing the normalized diffusion-sensitising gradient orientations. In SE-based sequences, the diffusion weighting is

$$b = \gamma G^2 \delta^2 \left(\Delta - \frac{\delta}{3}\right), \tag{13}$$

where γ is the gyromagnetic ratio (2.765 x 10^8 rad/s), G is the amplitude of the diffusion-sensitizing gradient, δ is the duration of the diffusion gradient, and Δ is the time interval between the diffusion gradients, also referred to as the diffusion time (see also Figure 5). Diffusion weighting can thus be increased by strengthening the gradient G, increasing the duration of the diffusion gradient δ, and increasing the diffusion time Δ.

2.3.2.2 Diffusion-sensitizing gradients

Several procedures have been used to optimize the parameters of the diffusion sensitizing gradients: the gradient orientation and the number of gradients applied (Papadakis et al. 1999, Papadakis et al. 2000, Jones 2004). A uniformly 3D-spaced diffusion-sensitizing gradient scheme is currently most commonly used and generally accepted as optimal (Jones et al. 1999a, Papadakis et al. 1999, Skare et al. 2000). The distributions of directions have been optimized, for example, by means of electrostatic repulsion schemes (Jones et al. 1999a) and polyhedaral schemes (Conturo et al. 1996, Hasan et al. 2001).

Typically, 20 directions are recommended for robust estimation of FA, and 30 directions for MD and tractography (Jones 2004). In some special applications, such as anatomical connections between brain areas with more complex structure and fiber crossings, even hundreds of directions have to be recorded. However, these applications are beyond tensor model, and more sophisticated methods, such as high-angular resolution diffusion imaging (HARDI), are applied instead.

2.3.3 Image analysis and parameter images

Raw diffusion-weighted images are rarely informative as such. Therefore, diffusion-weighted images are usually post-processed on a voxel-by-voxel basis to obtain parameter images that characterize the properties of the diffusion in the tissue, for example the strength of diffusion, the anisotropy degree, and the direction of diffusion.

2.3.3.1 Tensor model

The direction of diffusion can be defined by first calculating a diffusion tensor $\boldsymbol{D}$, a mathematical model for 3D diffusion, by using the measured DW-images (Basser et al. 1994b)

$$\boldsymbol{D} = \begin{matrix} D_{xx} & D_{xy} & D_{xz} \\ D_{yx} & D_{yy} & D_{yz} \\ D_{zx} & D_{zy} & D_{zz} \end{matrix}, \quad (14)$$

where $\boldsymbol{D}$ is a 3 x 3 symmetric, positive definite matrix. Several numerical methods exist for forcing the tensor to be positive definite, such as Cholensky, Log-Cholensky, and Log-Euler methods, as well as for solving the diffusion tensor robustly, *e.g.* maximum likelihood, linear and nonlinear least squares, and Bayesian methods (Koay 2011).

The diagonalization of the tensor by means of eigenvalue decomposition results in eigenvectors (v1, v2, v3) and eigenvalues (λ_1, λ_2, λ_3), which represent the direction and strength of diffusion along three orthogonal directions, respectively. Figure 7 presents the eigenvectors as ellipsoids: the symmetric sphere means isotropic diffusion (left panels), whereas anisotropic diffusion results in an ellipsoid whose axis, the principal eigenvector, is typically assumed to represent the direction of strongest diffusion (right panels) (Basser et al. 1994b, Basser et al. 1994a). Moreover, Figure 8 shows an FA image (left panel) with isotropic diffusion in ventricles as spheres, and anisotropy in white matter of the splenium of the corpus callosum as flattened ellipsoids (right panel).

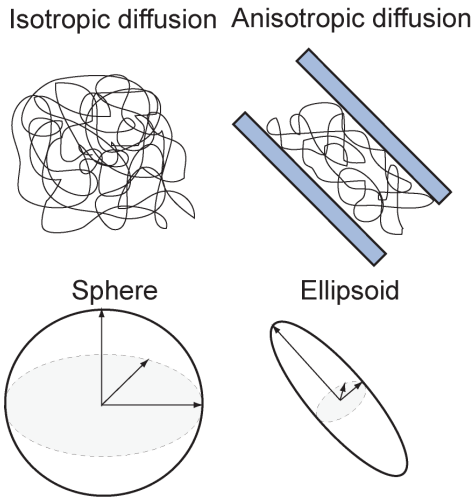

Figure 7: Isotropic (*top left panel*) and anisotropic (*top right panel*) diffusion. The *blue color* indicates tissue structures that restrict and hinder diffusion. Isotropic diffusion can be characterized as symmetric sphere (*bottom left panel*) whereas anisotropic diffusion is an ellipsoid (*bottom right panel*) whose main axis represents the direction of diffusion. Figure from Hiltunen et al. (2007) with the courtesy of Duodecim.

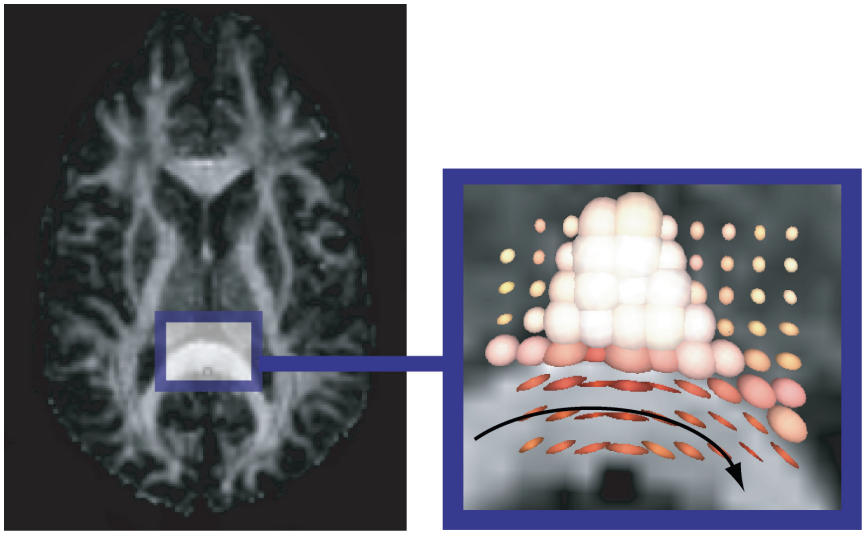

Figure 8: Visualization of the direction of diffusion with ellipsoids. Diffusion in the brain area surrounded by the blue box (*left panel*) is visualized with ellipsoids (*right panel*). The brain area includes the fibers of the splenium of the corpus callosum, parts of ventricles, and gray matter. Higher anisotropy is shown as red, flattened ellipsoids. *Black arrow* shows the direction of strongest diffusion and thereby the direction of a fiber bundle. Figure from Hiltunen et al. (2007) with the courtesy of Duodecim.

The tensor model assumes that a single population of fibers within a voxel runs in the same orientation. Even though this is not exactly true due to the complexity of neuroanatomical structures, the tensor model serves as a good approximation in many applications utilizing diffusion of water molecules. Moreover, several more advanced methods have been introduced for modelling more complex neuroanatomical structures, such as HARDI (Frank 2001), diffusion spectrum imaging (DSI) (Wedeen et al. 1999, Wedeen et al. 2001), Q-ball imaging (Tuch et al. 2003, Tuch 2004), spherical convolution (Anderson and Ding 2002, Tournier et al. 2004), and persistent angular structure MRI (PASMRI) (Jansons and Alexander 2003).

All these approaches aim to resolve the multiple fiber orientations within the voxel by means of orientation distributions of fiber populations on the basis of multiple recordings. DSI utilizes typically 300–500 recordings, acquired in many directions with multiple b-values up to 17000 s/mm^2, whereas Q-ball imaging, spherical convolution, and PASMRI apply multiple gradient directions (less than DSI) with the same, constant b-value, thus providing a more simplified approach than DSI. Morever, q-space imaging (QSI), composite hindered and restricted

model for diffusion (CHARMED), and diffusion kurtosis imaging (DKI) in turn assume that the measured diffusion signals (with several b-values) consist of compartments, *i.e.* free, hindered, and restricted diffusion components (Assaf and Cohen 1998, Assaf and Basser 2005, Jensen et al. 2005). The obtained signals are modelled with multiple exponential decays instead of a single exponential decay and/or provide quantification of the degree to which diffusion is non-Gaussian.

2.3.3.2 Processing DTI data

The diffusion tensor as such is not, neither in numerical (matrix, Eq. 14) nor graphical (ellipsoid, Figure 8) form, optimal for the visualization of diffusion. Therefore, tensor information is typically further processed and visualized in the form of scalar parametric maps, such as mean diffusivity (MD), fractional anisotropy (FA), and direction-encoded color (DEC) map.

Mean diffusivity (MD)

Figure 9 (left panels) shows an example of MD maps to quantify the strength of diffusion (Basser and Pierpaoli 1996)

$$MD = \frac{\lambda_1 + \lambda_2 + \lambda_3}{3} \tag{15}$$

by means of eigenvalues λ_1, λ_2, and λ_3. MD in cerebrospinal fluid (CSF) is about 3 x 10^{-3} mm^2/s, whereas in healthy brain tissue, MD is about 0.7 x 10^{-3} mm^2/s, without a clear contrast between gray and white matter (Le Bihan et al. 2001).

Fractional anisotropy (FA)

Fractional anisotropy (FA) in Figure 9 (middle panels) shows the degree of anisotropy in tissue by means of eigenvalues λ_1, λ_2, and λ_3 (Basser and Pierpaoli 1996, Pierpaoli and Basser 1996)

$$FA = \sqrt{\frac{1}{2}} \frac{\sqrt{(\lambda_1 - \lambda_2)^2 + (\lambda_2 - \lambda_3)^2 + (\lambda_3 - \lambda_1)^2}}{\sqrt{\lambda_1^2 + \lambda_2^2 + \lambda_3^2}} \tag{16}$$

and is thus independent of local fiber orientation. Diffusion is strongly directional in the bright areas of Figure 9 (middle panels), but approximately symmetric in all directions in the dark areas. FA is highest in major white matter tracts with a maximum theoretical value of 1, low (0.1–0.2) in gray matter, and approximately 0 in CSF.

Direction-encoded color (DEC) map

One informative way to visualize the direction of diffusion is a direction-encoded color (DEC) map in which the principal eigenvector is presumed to represent the fiber orientation in a voxel. Each component (*x, y, z*) of the eigenvector is assigned to a different color, *e.g.* red, blue, green, and the resulting image is weighted by FA to exclude the tissues with low-anisotropy diffusion (Pajevic and Pierpaoli 1999). The resulting image is thus an FA-weighted vector component image.

In Figure 9 (right panels), the DEC maps show the directions of anisotropic structures in different colors. Some clear anatomical structures are labelled in the DEC-images according to an atlas of white matter structures of the human brain (Mori et al. 2005).

Anatomical information in DEC maps can be used in quantitative DTI analysis so that the coordinates of regions of interest (ROIs), identified from the DEC map, are superimposed on the coregistered MD and FA maps. Values within the ROIs are then extracted and subjected to further analysis.

Group-level analysis of parameter images

Earlier, DTI parameter maps were mainly analyzed on an individual-subject basis using visual inspection of images and ROI analysis. In ROI analysis, values of parameter maps, typically MD and FA maps, are extracted from selected brain (or other anatomical) areas. However, the ROI analysis is observer-dependent and time-consuming, requiring frequent input from the analyzer. More automatic and objective methods would therefore be desirable. On that basis, voxel-based analysis (VBA), developed originally for similar analyses of anatomical T1-weighted MR images, has at present increasingly been applied to address group-level differences in DTI parameter images. A clear advantage of VBA, compared with ROI- or tractography-based analyses, is that the whole brain can be studied rather automatically without the need for *a priori* knowledge about tracts to be tested. Also, VBA is assumed to be able to detect small, disease-related changes that are still invisible to a radiologist.

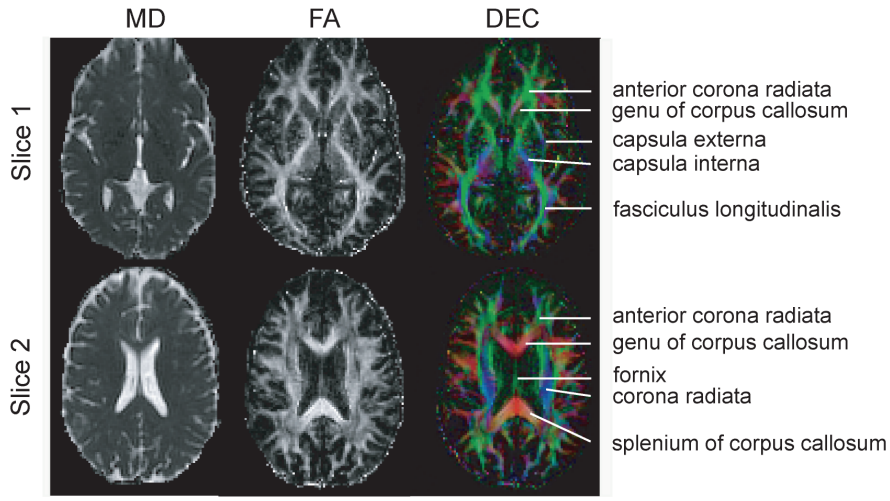

Figure 9: Mean diffusivity (MD, *left panels*) describing the strength of diffusion, anisotropy maps (FA, *middle panels*), and direction-encoded color (DEC, *right panels*) maps in two different axial brain slices. MD in gray and white matter is approximately equal thereby showing no contrast. In FA maps, strongly oriented diffusion in white matter is shown as bright, whereas isotropic diffusion in gray matter is dark. DEC maps show structures of different orientation with different colors: red – right-left, green – anterior-posterior, and blue – superior-inferior. As an example, a few anatomical structures have been labeled. Figure from Hiltunen et al. (2007) with the courtesy of Duodecim.

Conventional voxel-based analysis (VBA) with SPM

VBA, applied to DTI, was first adopted rather directly from its original application to anatomical MR image analysis. The VBA analysis chain for DTI consists of correction for motion and eddy currents, spatial normalization, smoothing, and statistical voxel-by-voxel analysis. The processing steps in VBA, described in more detail in the sequel, aim to enhance the images to obtain higher statistical power in the statistical analysis. Several computer programs exist for VBA, among which Statistical Parameter Mapping (SPM, Wellcome Department of Cognitive Neurology, London, UK), mainly used for VBA of anatomical MR images and functional MRI analysis, is one of the most commonly used. In P2, we studied the sensitivity of conventional DTI–VBA with SPM.

Eddy currents originate from gradients that are used for diffusion sensitizing and for the spatial encoding of MRI signals. When gradients are switched on and off rapidly, undesired currents spread to all conducting structures

of the MRI scanner and produce residual magnetic fields that distort images. In DTI, the strength and appearance of distortions vary depending on the directions of diffusion-sensitizing gradients. In practice, the images shear, scale, and shift differently, and voxels in different diffusion-weighted images are not coregistered. To correct these distortions and small subject movements, linear affine transformations are usually used with non-diffusion-weighted b_0-image as reference image during registration. Next, the images are subjected to spatial normalization to deform the individual brain images into a standard anatomical space for inter-individual comparisons. In spatial normalization, affine transformation alone, or affine transformation followed by non-linear warping has been used. The former transformation mainly fits the overall brain shape whereas the nonlinear warping also attempts to fit the inner structures. Typically, a non-diffusion-weighted b_0-image or anatomical T1-weighted image is used as the reference image that will be fitted into the template image (standard space), and the same parameters are then used for transforming DW or parameter (MD, FA) images into the same standard space.

The template (or reference) image used in the fitting may be a general template provided by the software or a study-specific template based on the user's own images. Earlier, DTI–VBA studies have commonly used the template provided by the Montreal Neurological Institute (MNI), implemented for example in SPM software (Borroni et al. 2007, Seok et al. 2007). One obvious disadvantage of the MNI templates is the lack of a T2-weighted EPI template. Instead, either a T2*-weighted EPI template with the same distortions but different contrast, or a T2-weighted template with the same contrast but different distortions has to be used; this may cause coregistration inaccuracies that affect the final statistical results. Therefore, study-specific templates (Guimond et al. 2000, Jones et al. 2002, Smith et al. 2006), or more recently introduced FA templates (Mori et al. 2008), would be preferable. The first one generally reduces the residual variance in coregistration, whereas the latter provides more suitable contrast for coregistration compared with the MNI template. Study-specific templates are mandatory in studies of children or of patients with degenerative diseases.

After spatial normalization, the images are typically filtered with an isotropic smoothing filter to further compensate for inter-subject anatomical variation and misregistrations, to assure normally-distributed data for statistical testing, and to fulfill the mathematical requirement of spatially-continuous imaging data assumed in correction for multiple comparisons.

Figure 10 shows an example of how MD (top panels) and FA (bottom panels) images change during preprocessing: original images (left panels) and

spatially normalized images (second panels from left) reveal anatomical information and a square-shaped artificial lesion, whereas normalized and smoothed images are more blurred (smoothing with 6-mm and 8-mm filter, (full-width at half maximum, FWHM); two rightmost panels).

Statistical tests are performed for each voxel separately. Both the MD and FA images are often tested using parametric tests, such as the t-test, although FA data are known to violate the assumption of Gaussianity and non-parametric approaches should be used instead (Jones et al. 2005).

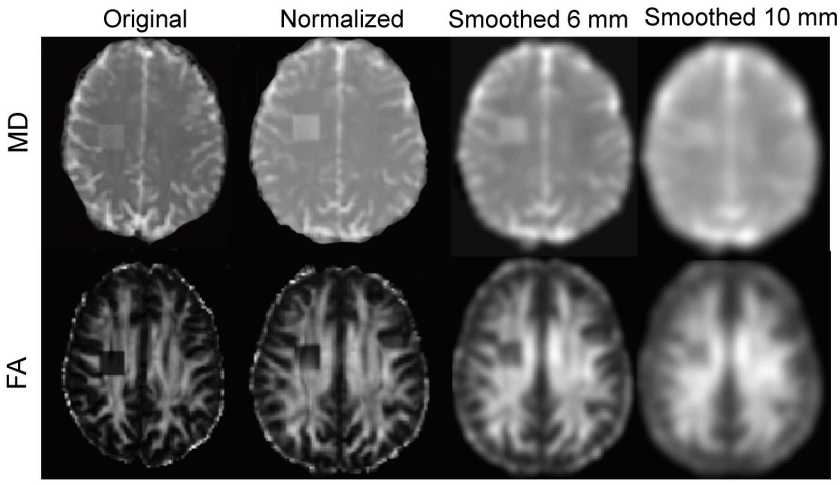

Figure 10: Examples of preprocessing of MD (*top panels*) and FA (*bottom panels*) images: original images (*left panels*), spatially normalized images (*second panels from left)*, and normalized and smoothed images; 6-mm smoothing kernel (*second panels from right*) and 10-mm smoothing (*right panels*). An artificial lesion has been positioned on MD and FA images (dark square in FA and bright in MD); lesions from P2.

Recent methodological improvements in VBA

Several methodological improvements have been suggested for DTI–VBA. Realignment of diffusion gradient directions (*i.e.* b-matrix) using motion-correction parameters improves the accuracy of diffusion measures and fiber orientation (Leemans and Jones 2009). Improved registration methods aim at utilizing the whole tensor information during spatial normalization, thereby requiring tensor reorientation (Alexander et al. 2001). This approach enhances the spatial and orientational alignment of the data (Alexander et al. 2001, Park et al. 2004, Van Hecke et al. 2007). Moreover, other improved methods, such as atlas-based

approaches at the individual subject level (Guimond et al. 2000, Jones et al. 2002, Park et al. 2004, Smith et al. 2006) or population/group level (Goodlett et al. 2006, Van Hecke et al. 2008) may give more reliable statistical results (Sage et al. 2009). In the subject-based approach, a single subject is used as the reference for the atlas, whereas in group-based atlases, all subjects' data contribute equally to the atlas. Subject-based atlases may thus contain biases due to the individual anatomy of the reference image if the differences are large compared with the other subjects (Wang et al. 2006, Van Hecke et al. 2008).

Filtering with an isotropic smoothing filter affects the results of VBA, as has been demonstrated in several studies (Park et al. 2004, Jones et al. 2005, Van Hecke et al. 2010). Park and coworkers (2004) studied hemispheric asymmetries in healthy subjects by means of FA using 3-, 6-, and 9-mm smoothing filters and showed differences in statistical values and extents of brain regions. Later, Jones and coworkers (2005) derived four different conclusions from the same imaging data (schizophrenia patients *vs*. healthy subjects) depending on the size of smoothing kernels, ranging from 3 mm to 16 mm in steps of 1 mm.

Lee and coworkers (2009) suggested a tissue-specific smoothing-compensated method that is based on segmentation of imaging data into tissue masks of gray matter, white matter and CSF prior to spatial normalization. These masks are then utilized to compensate the effects of spatial smoothing.

Moreover, recently, anisotropic Gaussian smoothing was found to increase VBA's sensitivity and specificity in detecting simulated pathologies in FA images (Van Hecke et al. 2010). In contrast to isotropic smoothing, the kernel size in anisotropic smoothing varies in different directions so that the smoothing kernel is shaped and scaled according to local image properties. In practice, these properties are revealed by eigenvalues and eigenvectors such that the imaging data are only smoothed in homogeneous areas along the edges, instead of across the edges (Sijbers et al. 1999).

Tract-based spatial statistics (TBSS)

A more recent approach for VBA-type analysis in DTI is tract-based spatial statistics (TBSS) (Smith et al. 2006, Smith et al. 2007). In this approach, the subjects' FA images are first transformed into a common anatomical space using nonlinear registration. The most typical subject's image, selected on the basis of numerical calculations, is used as a reference for coregistration. Next, the tract skeleton is calculated by averaging all registered FA images and by thinning the mean FA; this skeleton represents the centers of all tracts common to the

population under study. Registered FA images from each subject are then projected onto the skeleton in a direction perpendicular to the local tract direction; this procedure improves the projection accuracy because the FA values change more in the perpendicular than the parallel direction. The final projected FA values are obtained from the centers of the original FA images, and are further fed into voxel-wise statistics. As TBSS-processed data follow a Gaussian distribution, they can be analyzed by means of parametric statistical tests.

2.3.3.3 Signal-to-noise ratio in DTI

Noise in diffusion-weighted images affects the eigenvalues and thereby causes bias in eigenvalue-derived parameter images (Pierpaoli and Basser 1996). Due to noise, the eigenvalues are unequal even in perfectly isotropic medium, and this discrepancy increases at higher noise levels. High noise levels increase spatial variance and increase the apparent anisotropy both in isotropic gray and anisotropic white matter (Jones and Cercignani 2010). These effects are slight at moderate SNRs, but increase as SNR decreases, making isotropic tissue to appear anisotropic (Pierpaoli and Basser 1996). Therefore, sufficient SNR is required for reliable DTI measurements. Several SNR levels have been proposed, such as SNR > 20 in b_0-image (Pierpaoli and Basser 1996), as well as SNR > 3:1 (Jones and Basser 2004), 10:1 (Descoteaux et al. 2009), and SNR $\geq 3/\exp(-b \times 10^{-3})$ in diffusion-weighted images; b is diffusion-weighting (Jones et al. 2013).

Noise may also cause negative bias in anisotropy and mean diffusivity due to Rician distribution of noise and thereby rectified noise floor related to the reconstruction of magnitude images (Jones and Cercignani 2010). Such bias can be obtained with insufficient SNR in b_0-image when moderate b-values are applied, and even with high SNR in b_0-image when high b-values are applied.

The general principles to increase the SNR in MRI are correct also for DTI (see Section 2.1.2.4 “Signal-to-noise ratio (SNR) in MRI”). The main practical actions to improve SNR in DTI are optimization of the voxel size, as well as the usage of a good receiver coil and parallel imaging. The voxel size has to be compromised so that it is large enough to provide a reasonable signal level, and small enough to guarantee a reasonable spatial resolution and minimal partial volume effect. Even though parallel imaging speeds up the scanning at the expense of SNR, it should be applied in DTI. As a whole, the shortened minimum TE overcompensates the loss of SNR, and the decreased TE generally improves the image quality by reducing distortions.

2.3.4 Tractography

The orientation and 3D course of fiber tracts can be visualized with tractography (Conturo et al. 1999, Jones et al. 1999b, Mori et al. 1999, Basser et al. 2000, Poupon et al. 2001, Parker et al. 2002, Tench et al. 2002, Parker et al. 2003). As an example, Figure 11 shows the tractography of the corpus callosum and corticospinal tract. It is typically assumed that the principal eigenvector represents the direction of the fiber tract within the voxel. However, several deterministic (*i.e.* streamline) and probabilistic tractography methods exist, as described briefly below.

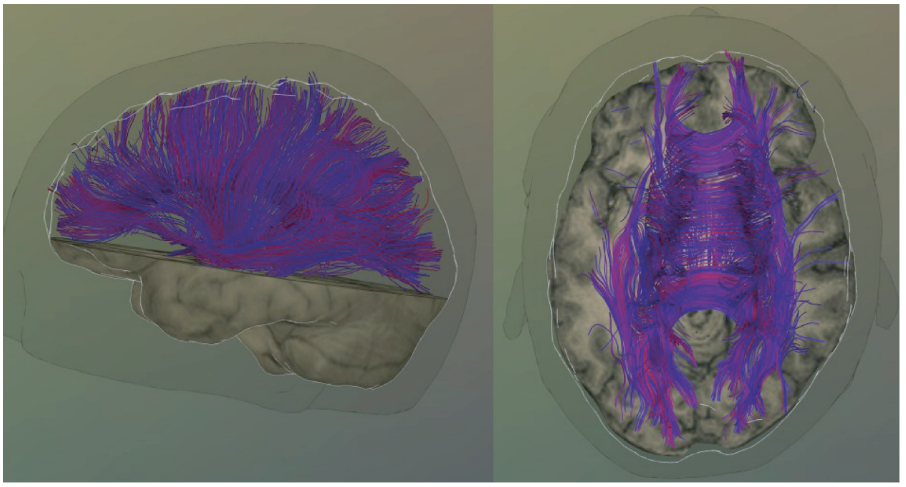

Figure 11: An example of tractography showing mainly fibers of the corpus callosum and corticospinal tract in the upper part of the brain. All voxels with FA > 0.7 were used as ROIs, and tracking was continued until FA fell below 0.2. Tracts are shown with registered T1-weighted anatomical images. Figure from Hiltunen et al. (2007) with the courtesy of Duodecim.

2.3.4.1 Deterministic tractography

In tract propagation, the fiber orientation in the seed voxel (or rather in an ROI consisting of several voxels) is estimated based on principal eigenvector or on the diffusion tensor. The tract is then propagated from voxel to voxel on the basis of the tensor/eigenvector (Conturo et al. 1999, Mori et al. 1999, Basser et al. 2000). The discrete vector information within the voxel is typically converted into continuous coordinates for more accurate tract propagation. Moreover, tracts can be propagated in small steps to provide more accurate tracking and a more realistic, smooth appearance of the tract. Several approaches have been proposed for step estimation such as Fibre Assigning by using Continuous Tracking (FACT) (Mori et al. 1999, Xue et al. 1999), Euler integration (Conturo et al. 1999), and Runge-Kutta (Basser et al. 2000) methods. Both FACT and Euler integration are piecewise linear methods with constant (Euler) or varying (FACT) stepsize, whereas Runge-Kutta is a nonlinear method utilizing higher-order integration and continuous derivatives which is especially advantageous for steeply-curved tracts.

The fiber tract is followed in both directions from a seed point until the tracts are finally combined. The tracking is stopped when certain stopping criteria, for example a threshold FA or angle between adjacent eigenvectors is achieved. Voxels below a chosen FA value, for example < 0.2–0.3, are considered to indicate isotropic diffusion without coherent fiber orientation. A typical angle threshold for adjacent eigenvectors is 35–45°, since image resolution in DTI is not high enough for reliable tract propagation at larger tract curvatures that may introduce errors to tracking results: for example, tracking can escape to an adjacent tract (Mori 2007).

Tractography results obtained with deterministic tractography often contain errors due to the partial volume effect, noise, or crossing fibers. These errors can be completely unknowable, thus weakening the confidence of the results, or they can be visible as incomplete tracts or single, clearly erroneous fibers escaping from the major tract. To correct for these errors, analysis parameters can be adjusted, a multi-ROI approach can be applied so that fibers including or excluding the ROIs are tracked (Mori et al. 2002b), or more advanced tractography methods can be used. Such advanced methods include, for example, tensor deflection (Lazar et al. 2003), regularization methods (Parker et al. 2000), Gibbs-tracking (Kreher et al. 2008), and probabilistic methods. Of these, probabilistic tractography methods provide quantification of the uncertainty of tracking results.

2.3.4.2 Probabilistic tractography

The orientation information in recorded diffusion-weighted images always has uncertainty resulting from noise, limited image resolution, and crossings of fiber tracts. The impact of these orientation uncertainties can be considered by defining probability density functions (PDFs) for fiber orientation. PDFs describe the expected distribution of possible fiber orientations on the basis of DW images. PDFs can be defined locally for each voxel (Behrens et al. 2003, Jones 2003, Parker et al. 2003), or additional information can be taken into account from the local neighbourhood voxels or from the entire tract (Jbabdi et al. 2007). Several approaches for defining PDFs have been proposed, such as bootstrapping (Jones 2003), Bayesian methods (Behrens et al. 2003, Behrens et al. 2007), and calibration using synthetic test functions (Parker and Alexander 2003, Parker and Alexander 2005). Once PDFs have been defined, a variety of methods can be used to generate a tract from voxel to voxel through the PDFs (Koch et al. 2002, Parker et al. 2002, Parker et al. 2003, Tournier et al. 2003). Of these, the Monte Carlo streamline approach runs a deterministic streamline process many times (*e.g.* 10 000 (Toosy et al. 2004)) to test for possible pathways from a single seed point (Koch et al. 2002, Parker and Alexander 2003). Front propagation methods in turn attempt to find pathways from the seed region through the brain by means of PDFs and a region-growing type of algorithm (Parker et al. 2002, Tournier et al. 2003). As a result of probabilistic tractography, each connection is assigned an index of connectivity (with a seed point); on the basis of these indices inferences about probabilities of connection may be made (Tournier et al. 2003, Parker 2004).

2.4 DTI applications

This Section briefly describes DTI applications, typical findings, and the effect of subject age on MD and FA. Imaging of peripheral nerves is presented to the extent required for understanding the background and results of this thesis.

2.4.1 Assessing white matter tracts

The main applications of DTI so far have been both in basic research and in clinical studies of white matter in the human brain; for reviews, see recent books by Johansen-Berg and Behrens (2009) and Jones (2011). In basic research, important methodological developments have taken place, for example, in fiber tracking methods and in solving the problem of crossing fibers. Moreover, advances have been made in forming maps of brain connectivity on the basis of DTI data.

DTI has been applied to various diseases affecting the brain's white matter tracts, such as Alzheimer's disease, multiple sclerosis, amyotrophic lateral sclerosis, ischemic stroke, epilepsy, tumors, brain injuries, and psychiatric diseases/schizophrenia. In most of these applications, the diseased brain areas and their connections have been searched or monitored by means of MD and FA to clinically evaluate their spatial location and extent, as well as the phase of the disease. Findings in normal-appearing brain areas and findings excluding certain brain areas may be helpful to a clinician for diagnostics and prognosis of disease.

Tractography has been advantageous in noninvasive visualization of white matter tracts (Catani et al. 2002, Wakana et al. 2004), in segmentation of tracts of interest for further analysis of diffusivity and anisotropy (Jones et al. 2005), and in pre-operative planning for patients suffering from brain tumors or other lesions to show the course of the fiber tracts at or near the surgery area (Mori et al. 2002a, Yu et al. 2005).

In addition to the brain, DTI has also been used for imaging the spinal cord (Clark and Werring 2002, Wheeler-Kingshott et al. 2002), kidneys (Ries et al. 2001), heart (Reese et al. 1995, Dou et al. 2002), muscles (Sinha and Yao 2002), and peripheral nerves (see Section 2.4.4 below). The main parameters of interest in these DTI studies are MD and FA, as well as tractography for visualizing the 3D course of tracts or nerves.

2.4.2 Typical findings in DTI

Increased MD and reduced FA are the most common findings related to brain pathologies (Horsfield and Jones 2002, Beaulieu 2009, Bodini and Ciccarelli 2009) and injured skeletal muscles (Zaraiskaya et al. 2006).

Increased MD may be due to inflammation and edema, whereas decreased FA may reflect damaged tissue structure, demyelination, axonal loss or increased isotropic water volume (Beaulieu 2009, Bodini and Ciccarelli 2009). Decreased MD and increased FA may be caused by acute ischemic events in tissue, whereas decreased MD and FA may be due to gliosis (Pierpaoli et al. 2001, Sotak 2002).

2.4.3 Effect of subject's age

Diffusivity decreases and anisotropy increases in brain white matter throughout childhood up to young adulthood (Mukherjee et al. 2001, Engelbrecht et al. 2002, Hermoye et al. 2006) because of decrease in water content in the cells, myelination, and a more organized architecture of nerve fibers (Neil et al. 1998, Hermoye et al. 2006). Changes in diffusivity and anisotropy are local and show regional variation (Huppi et al. 1998, Mukherjee et al. 2001, Righini et al. 2003, Partridge et al. 2004): rapid changes occur in tightly packed and early maturating commissural tracts (*e.g.* corpus callosum) and deep projection tracts (*e.g.* cerebral peduncle, internal capsule), whereas moderate changes occur in subcortical projection and association tracts (Partridge et al. 2004, Hermoye et al. 2006). Generally, the maturation-related changes in diffusivity and anisotropy are most rapid during the first 12 months of life, followed by slower changes during the second year, and reaching relatively stable, near-adult values after the age of 24 months (Hermoye et al. 2006, Provenzale et al. 2007). However, infants born preterm have decreased FA in several white-matter regions at the age of 15 years, compared with the matched control group of full-term infants and another matched group of full-term but small infants; these low FA values may be due to reduced myelination (Vangberg et al. 2006).

From adulthood to old age, the diffusivity increases and anisotropy decreases (Gideon et al. 1994, Virta et al. 1999, Salat et al. 2005a, Salat et al. 2005b, Sullivan et al. 2006, Sullivan et al. 2010). These age-related changes in white matter are regionally variable: they are generally greater in frontal and parietal areas, and smaller in occipital and posterior areas suggesting that later-

maturating areas might be more sensitive to age-related degeneration (Salat et al. 2005b, Sullivan et al. 2010).

2.4.4 Imaging of peripheral nerves

Earlier, peripheral nerves have mainly been imaged using MRI neurography that utilizes T2-weighted fast spin-echo (FSE) sequences with fat saturation (Filler et al. 1993) and T1-weighted sequences (Filler et al. 1996). In clinical MRI of peripheral nerves, T1-weighted spin-echo sequences with and without intravenous contrast agent, and T2-weighted short-tau inversion recovery (STIR) or fat-saturated T2-weighted sequences have been used (Jarvik et al. 2000, Jarvik and Yuen 2001, Grant et al. 2004, Jarvik et al. 2004). T1-weighted images show the fine anatomical structure of nerves, and the visibility of mass lesions can be improved by using contrast agents. T2-weighted images are generally advantageous in showing pathologies, for example, injured peripheral nerves may show up as hyper-intense (Grant et al. 2002, Grant et al. 2004).

Moseley and coworkers (1991) were the first to report diffusion anisotropy in the human tibial nerve, computed on the basis of diffusion coefficients. This work was done, however, before actual DTI was invented, and at that time, this research topic did not proceed further. Since peripheral nerves are of interest in our research group, we made an effort to image distal peripheral nerves by means of DTI (P3). Further, as a continuation for P3, we started to study whether DTI has clinical significance in the entrapments of distal peripheral nerves, concentrating on the median nerve in the upper limb, most often vulnerable to entrapments (P4).

When our feasibility study P3 succeeded and was in reporting phase, the first tractography study on thick sciatic nerve was published (Skorpil et al. 2004). Between completion of this thesis' publications P3 and P4, the first DTI feasibility studies on nerve injuries were published (Meek et al. 2006, Kabakci et al. 2009, Takagi et al. 2009), and later, the first studies on carpal tunnel syndrome were reported (Kabakci et al. 2007, Khalil et al. 2008, Stein et al. 2009). Simultaneously with P4, several other DTI studies of peripheral nerves were published.

Carpal tunnel syndrome

Carpal tunnel syndrome (CTS) is a common neuropathy caused by entrapment of the median nerve. The symptoms include decreased sensation, tingling or numbness, and pain in the upper extremity (Jarvik and Yuen 2001, Jarvik et al. 2004). Currently, the diagnosis is based mainly on clinical examination and electrophysiological findings. Other imaging methods, such as MRI neurography, DTI, and ultrasound, have also been suggested for CTS diagnostics. However, due to their poorer availability and specificity compared with the gold standard electrophysiological recordings, these methods are typically used additionally to exclude other pathologies that might contribute to CTS symptoms.

Findings of MRI neurography in CTS include increased cross-sectional area of the median nerve within and proximal to the carpal tunnel, bright signal within the nerve in T2-weighted images, swelling of the nerve either distal or proximal to the point of maximal compression, flattening of the nerve within the tunnel, and thickening and high signal intensities in flexor tendon sheets and deep palmar bursa (Monagle et al. 1999, Cudlip et al. 2002, Jarvik et al. 2002).

In ultrasound measurements, the most frequent finding in CTS is increased median-nerve cross-sectional area, although inconsistencies exist regarding the classification between normal and abnormal values, general sensitivity of the method, and anatomical location of the measurement (Seror 2008, Roll et al. 2011, Cartwright et al. 2012, Mhoon et al. 2012).

3 Objectives

The objectives of this thesis were

- to quantify the mechanical vibrations during DTI to find out whether vibration strengths vary in different parts of the MRI scanner and its surroundings (P1)

- to evaluate the performance of conventional voxel-based analysis (VBA) using simulated brain lesions in mean diffusivity (MD) and fractional anisotropy (FA) images of healthy subjects (P2)

- to study whether distal peripheral nerves can be imaged by means of DTI, and to optimize the scanning and analysis parameters (P3)

- to monitor by means of DTI the pre- and post-operative integrity of the median nerve in patients suffering from carpal tunnel syndrome (P4)

4 Summary of Experiments

This Chapter summarizes publications P1–P4 by describing briefly their backgrounds, motivations, and methods, as well as the main results and brief conclusions.

All magnetic resonance images were acquired with a 3T MRI scanner (Signa VH/i, upgraded to Signa HDxt, GE Healthcare, Chalfont St Giles, UK) using a quadrature head coil (P1) and an 8-channel brain-array head coil (P2) for brain imaging, and a wrist coil (wrists in P3) and an extremity coil (knee and ankle in P3, wrists in P4) for imaging of extremities. We applied two SS-SE-EPI sequences for DTI with spectral spatial RF-pulse for fat suppression, and prior to the DTI series, high-order shimming was applied to reduce the inhomogeneities of the main magnetic field. The vendor-supplied sequence was tested in P1, and the other sequence was applied in P2–P4.

Informed consent was obtained from all subjects in P2–P4, and the studies had the prior approval of the Helsinki and Uusimaa Hospital District Ethics Committee.

4.1 DTI-related mechanical vibrations are unevenly distributed in the scanner (P1)

Background and motivation: During DTI scanning, subjects can clearly sense mechanical vibrations, likely originating from diffusion-sensitizing gradients. It has been generally assumed that these vibrations are of the same strength and phase in all parts of the MRI scanner and can thus be ignored. We quantified mechanical vibrations during DTI from several parts of MRI scanner and its surroundings to see whether vibrations can affect the image quality.

Methods: An optical laser-based interferometer (Polytec 3000, Polytec GmbH, Germany) was used for quantifying vibrations. The interferometer measured the motion of the surface at the measurement point. The motions were registered as a Doppler shift, proportional to the velocity of the moving surface. The measurement points were covered with reflection tape for the laser beam to allow separate recordings in x- (right–left), y- (up-down), and z-directions (along the magnet bore); a prism was used in x- and y-directions. The test outputs for

gradient power supplies and velocity signals from the interferometer were connected to an oscilloscope to record the signals within the same timescale.

Imaging: We measured altogether 7 diffusion gradient directions to test each gradient axis (*x, y, z*) separately and to test the combinations of gradient axes (*xy, xz, yz, xyz*) with b = 50, 500, 1000, 2000, and 3000 s/mm^2. Data were recorded from 22 axial slices of 3.5 mm thickness. Other imaging parameters were: TR = 15 000 ms, TE = 78–108 ms, FOV = 24 cm, matrix 128 × 128. Measurements were performed with a spherical phantom positioned in the head coil, with or without a subject in the patient bed. Twice-refocused spin-echo method was applied during the scanning in some series to reduce the distortions caused by eddy currents.

Data analysis: The vibrometer voltage signal outputs were analyzed using Matlab (version 6.5, MathWorks, Inc., MA); the signals were converted to velocity signals and were further integrated numerically to quantify the movement. We focused our quantification to the readout period during which the movements were at their largest, as shown in Figure 12.

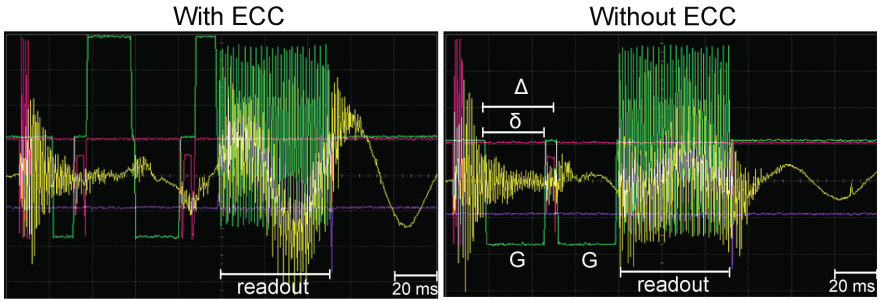

Figure 12: Vibration measurements (oscilloscope screen) with (*left panel*) and without (*right panel*) ECC when quantifying vertical movement of body coil with respect to a phantom in the head coil. *Pink lines* – slice selection gradient, *green* – frequency encoding/readout gradient, *violet* – phase encoding gradient, *yellow* – vibrometer output signal (velocity function, 1 vertical division corresponds to 1 V = 5 mm/s).

Results: In contrast to the general assumption that the DTI-related vibrations are of the same strength and phase in all parts of the scanner and can thus be ignored, our results in Figure 13 and 14 show that vibrations are distributed unevenly in the scanner structures and should thus be taken into consideration. Figure 13 and Figure 14 show clearly that vibration-related movements increased with b-value (*i.e.* diffusion-weighting), the number of diffusion-sensitizing gradients (*x, y, z, xy, xz, yz, xyz*), the usage of online eddy-current correction (ECC; on/off), and with weight on the patient table. The online ECC enhanced the

vibrations by at least a factor of 1.5 (b = 1000 s/mm^2) and by 3 (b = 3000 s/mm^2), as is evident from Figure 14 (right panel).

Conclusion: The presence and effect of mechanical vibrations during DTI scanning should be acknowledged. Adjustment of the b-value and selection of a diffusion-sensitizing gradient scheme are the easiest way to decrease the vibration level.

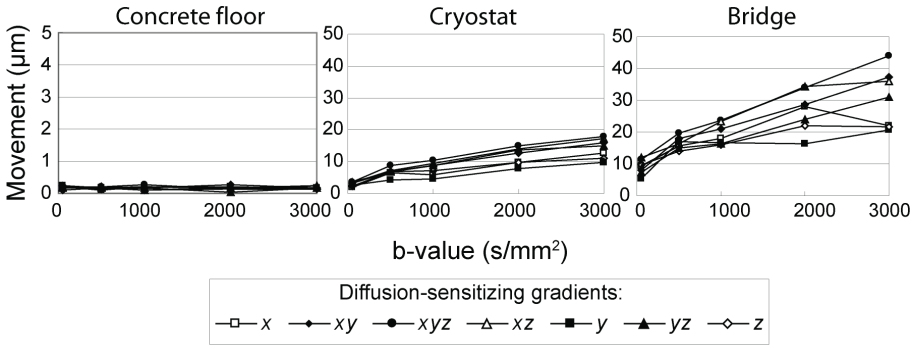

Figure 13: Vibration-related movement at different points in the MRI scanner and surroundings as a function of b-value. Measurement points on the concrete floor (*left panel*), cryostat (*middle panel*), and bridge (*right panel*) are shown with different combinations of diffusion-sensitizing gradients.

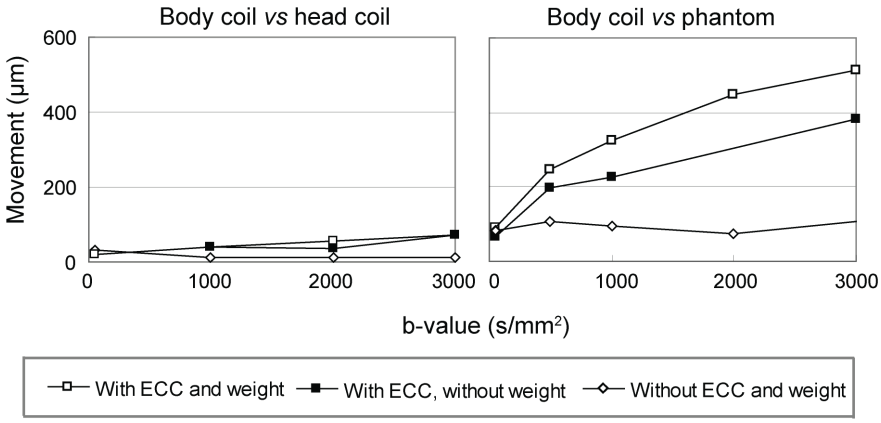

Figure 14: Vibration-related movements of the body coil with respect to the head coil (*left panel*) and with respect to a phantom in the head coil (*right panel*) as a function of b-value. Three measurement conditions demonstrate the movements without ECC and weight, with ECC and without weight, and with weight and ECC.

4.2 Preprocessing affects the results of DTI–VBA (P2)

Background and motivation: Today, a growing trend in DTI analysis is VBA to address differences in diffusivity and anisotropy maps at group level. Although methodological improvements have already been proposed for DTI–VBA, no systematic studies exist regarding the performance of mainstream DTI–VBA applications analyzed with statistical parametric mapping (SPM) without such improvements. We thus employed controlled simulated lesions to determine how the VBA analysis chain affects the sizes and intensity values of the detected lesions. In addition, we specified detection thresholds for the extent and intensity change of lesions that can be found with certain statistical criteria.

Methods: Twenty healthy subjects (aged 29 ± 5 years) participated in the study. To simulate artificial lesions, we increased MD and decreased FA—the most typical abnormalities in brain pathologies—in superior longitudinal fasciculus (SLF), corticospinal tract (CST), and body of corpus callosum (CC). The sizes of these simulated lesions, computed with Matlab software (MathWorks, Inc., MA), varied from 10 to 400 voxels (10, 25, 50, 100, 200, 300, 400), each 10.5 mm^3 in size, corresponding to volumes of 106–4219 mm^3. Intensity changes varied from 10% to 100% (10%, 30%, 50%, 75%, and 100%).

Imaging: For DTI, we measured 52 axial slices of 3 mm thickness, with 8 diffusion gradient orientations, b = 1000 s/mm^2; the gradient scheme compensated for the cross-terms of imaging and diffusion-sensitizing gradients (Neeman et al. 1991). The other imaging parameters were: TR = 12 000 ms, TE = 78 ms, FOV = 24 cm, matrix 128 × 128, number of replications = 8 times. In addition to DTI, a T1-weighted 3D spoiled gradient echo (SPGR) sequence in the axial direction was applied with 1-mm isotropic resolution.

Data analysis: FSL software (version 4.0, www.fmrib.ox.ac.uk/fsl) was applied to correct for subject movement and eddy currents, to remove the non-brain structures with the Brain Extraction Tool (BET), and to compute the MD and FA maps with the DTIFit program.

The VBA consisted of spatial normalization, smoothing, and statistical analysis. The parameters for spatial normalization were estimated by fitting the b_0-image of each subject into standard anatomical space (MNI, Montreal Neurological Institute) using the EPI template and affine and nonlinear transformations in SPM2 (Wellcome Department of Cognitive Neurology, London, UK). These normalization parameters were applied to MD and FA images that were further filtered with 0 mm (no filtration), 4 mm, 6 mm, 8 mm, and 10 mm FWHM.

Differences in MD and FA maps, compared between lesion and non-lesion groups, were considered statistically significant if the voxels passed the height threshold of $p < 0.001$ or $p < 0.05$ (FWE-corrected; family-wise error rate correction).

The performance of VBA was studied

- *without any preprocessing effects:* lesions were positioned onto normalized FA and MD images, and lesion images (N = 20) were compared with the same images without lesion
- *with spatial normalization and smoothing:* lesion images (MD, FA) of each subject, created in individual imaging space, were spatially normalized and smoothed. Lesion (N = 20) *vs.* non-lesion images, obtained with the same transformation into standard space, were compared statistically
- *with spatial normalization and smoothing in the presence of inter-subject variation:* subjects were divided into two age- and gender-matched groups (N = 10 *vs*. N = 10), one with lesions and the other intact; the spatially normalized and smoothed images were statistically compared.

Results: Without preprocessing, the lesions were found rather well, and only the smallest lesions with 10% intensity change were not found robustly. Generally, in the presence of preprocessing, lesions with intensity changes of 10–50% and extent less than 50 voxels were not detected. Figure 15 shows an example how smoothing changed the intensities of lesion MD and FA images from the original values.

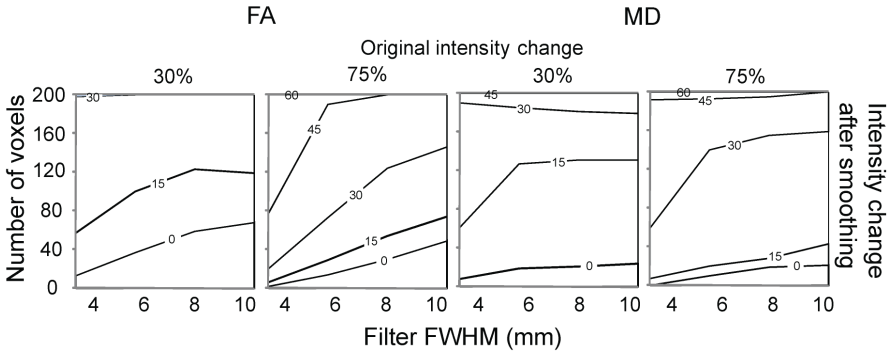

Figure 15: Smoothing changed the original voxel values within FA (*two left columns*) and MD (*two right columns*) lesions so that voxel values were remarkably lower than the original ones. The contour lines show the number of voxels and their intensity changes (marked as numbers within the lines) after filtering at 4 mm, 6 mm, 8 mm, and 10 mm (FWHM). Intensity changes of 30% and 75% are shown for a lesion size of 200 voxels in CST (single subject).

Detection thresholds varied between the three brain areas so that CST lesions were the easiest to detect, SLF lesions slightly worse, and CC lesions were always hardest to detect. Moreover, detection thresholds were generally lower for MD lesions than FA lesions. Spatial smoothing markedly enlarged the estimated lesion sizes and decreased the estimated intensity changes.

Figure 16 shows an example of the statistical result combined with an MD and FA image. Anatomical locations of detected lesions were accurate, whereas the estimated lesion sizes were mainly inaccurate so that small lesions were underestimated in size, and large lesions strongly overestimated, even up to ten times the original size.

Conclusion: Since preprocessing of VBA significantly affected the outcome of analysis, the impact of analysis steps should be verified before interpreting the findings. Analysis should also be carried out without smoothing.

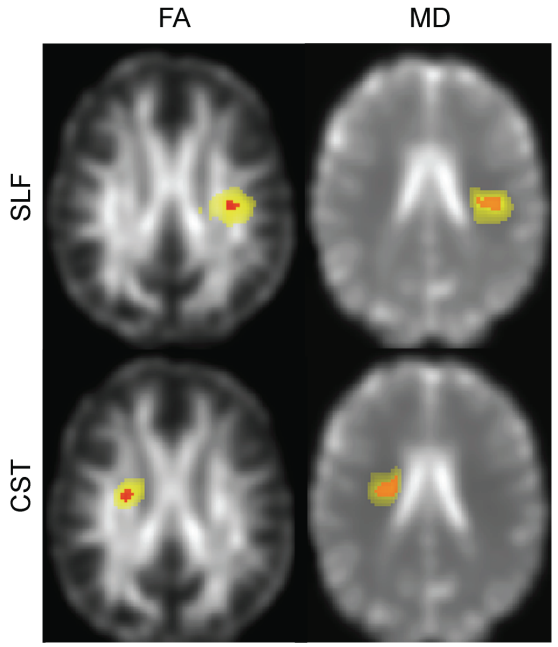

Figure 16: An example of DTI–VBA results of FA (left panels) and MD (right panels) images for SLF and CST (true lesion size originally 200 voxels, intensity change 30%, smoothing 8 mm). Two statistical thresholds were applied: yellow – $p < 0.001$, extent threshold 10 voxels; orange – $p < 0.05$, FWE correction.

4.3 DTI is able to track distal peripheral nerves (P3)

Background and motivation: No earlier DTI studies on distal peripheral nerves existed prior to this study. We studied whether distal peripheral nerves can be imaged with DTI and visualized with tractography.

Methods: Six healthy subjects (aged 22–36 yrs) participated in the study. Median, ulnar and radial nerves in 4 healthy upper limbs, and tibial and peroneal nerves in 3 healthy lower limbs, were imaged with DTI.

Imaging: For DTI, we measured 17–23 axial slices with 13 uniformly spaced gradient directions ($b = 1000$ s/mm^2) and a non-diffusion-weighted b_0 image. Other imaging parameters: TR = 5000–7000 ms, TE = 82–86 ms, number of replications = 3–4 times, slice thickness = 3.5 mm, FOV = 10–12 cm (wrist), 12 cm (ankle), and 14–16 cm (knee), matrix 64 × 64 (wrist and knee), and 96 × 96 (angle). Anatomical reference images were scanned with a gradient echo sequence.

Data analysis: ADC, FA and DEC maps and tractography of nerves were computed with dTV1.5 software (Image Computing and Analysis Laboratory, Dept. of Radiology, The University of Tokyo Hospital, Japan). An ROI was positioned on T2-weighted EPI image; the position was verified from DEC maps and anatomical reference images. Tracking was stopped when FA fell below 0.3 (lower limb) and below 0.4 (wrist).

Results: Figure 17 shows tractography results for upper and lower limb nerves. Median, ulnar, and radial nerves in upper limb, and tibial and peroneal nerves in lower limb corresponded well to known anatomy. The nerves were mainly tracked nicely, but in one of the four subjects, the radial nerve was untracked, and in the ankle area, only the tibial nerve was tracked, whereas the distal peroneal nerve remained untracked in all subjects.

Conclusion: DTI and tractography can be used to image and visualize distal peripheral nerves.

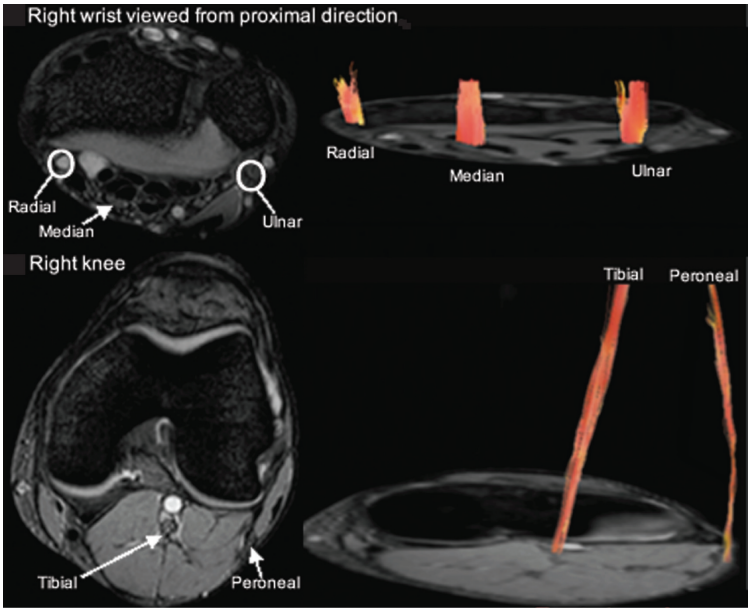

Figure 17: Tractography of distal peripheral nerves and corresponding anatomical images: (*top panels*) median, ulnar, and radial nerves in right wrist, viewed from proximal direction (FA > 0.4), and (*bottom panels*) tibial and peroneal nerves in knee, viewed from back (FA > 0.3).

4.4 Age and carpal tunnel syndrome cause similar DTI changes in median nerve (P4)

Background and motivation: As a continuation of our earlier methodological paper (P3), we applied DTI in patients with carpal tunnel syndrome pre- and post-operatively, and studied age effects in healthy age- and gender-matched subjects and in healthy young subjects.

Methods: Diffusivity (MD, eigenvalues) and FA images along the median nerve were compared in 12 patients (mean age 47 years) suffering from CTS, 12 age- and gender-matched controls (mean age 46 years), and 12 young control subjects (mean age 23 years). In these 12 patients, 21 of the 24 wrists were examined (1 severe CTS, 9 moderate, 6 mild, 4 previously operated, and 1 healthy wrist). Nine of the 12 patients were also scanned post-operatively. All hands underwent a clinical examination.

We compared FA and diffusivity between the groups, studied age effects in healthy matched and young groups, and correlated FA and MD with electrophysiological neurography measures. In addition to traditional analysis,

based on mean values of the whole nerve, we also extracted diffusivity and anisotropy values slice-wise and tested the feasibility of such slice-analysis for the diagnostics of individual patients. Post-operative follow-up was done approximately 1 year after the surgery. Test-retest reliability of MD and FA was studied preliminarily with five scans of one subject on different days.

Imaging: We measured the b_0-image and 33 axial slices with 25 uniformly spaced diffusion gradient directions (b = 1000 s/mm^2, diffusion gradient duration δ = 26 ms, diffusion time Δ = 34 ms). The other imaging parameters were as follows: TR = 10 000 ms, TE = 86 ms, number of replications = 3, slice thickness = 3 mm, FOV = 12 cm, and matrix 64 × 64. In addition to DTI, several anatomical sequences were scanned: T1- and T2-weighted images with fast-spin echo and/or gradient echo sequences, with and without fat suppression, and in axial and sagittal directions (for imaging parameters, see P4).

Data analysis: The maps for MD, parallel diffusivity along the nerve (first eigenvalue), perdendicular diffusivities (second and third eigenvalues) and tractography were calculated with DtiStudio (version 2.4.1; (Jiang et al. 2006)). A free-hand ROI for tractography was positioned on the median nerve in the DEC-map. Fibers coursing through the ROI were tracked from slice to slice as long as FA > 0.25 and the angle between adjacent eigenvectors was below 40 degrees. Minimum, maximum and mean diffusivity and FA values were extracted from tractography results slice-wise, and they were also averaged on the basis of anatomical location (proximal nerve, carpal tunnel, distal nerve). Two-sample t-tests (diffusivities), Mann-Whitney U tests (FA) and paired t-tests (pre- *vs*. post-operative patients) were used in statistical testing.

Results: Figure 18 (left panel) shows the MD values that were highest in pre-operative patients, 4% lower in matched controls, 10% lower in young controls, and 15% lower in post-operative patients. A similar pattern in diffusivity was present in carpal tunnel and distal nerves, and also in parallel diffusivity (first eigenvalue) and perpendicular diffusivity (second eigenvalue). No significant differences between the groups were observed in the proximal nerve. Perpendicular diffusivity, measured with the second and third eigenvalue, differed between pre- and post-operative patients (carpal tunnel and distal nerve).

The highest FA values, shown in Figure 18 (right panel), were obtained in young controls; FA values were almost equal in pre-operative patients and matched controls, and lowest in post-operative patients. FA differed significantly between pre-operative patients and young controls (carpal tunnel, distal nerve), post-operative patients *vs.* young controls, and matched controls *vs.* young controls.

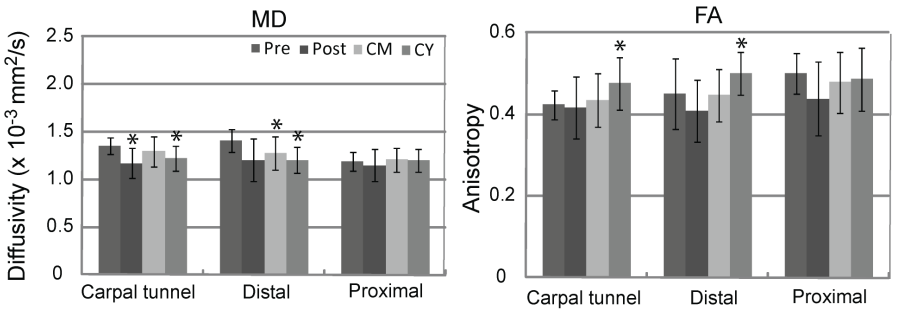

Figure 18: Mean ± SD MD *(left panel)* and FA *(right panel)* along the median nerve in distal nerve, carpal tunnel, and proximal nerve for pre-operative patients (Pre), post-operative patients (Post), matched controls (CM) and young controls (CY). Statistically significant (at least $p < 0.02$) differences compared with pre-operative patients are marked with an asterisk.

Figure 19 demonstrates that MD in carpal tunnel correlated positively and FA negatively with age. Comparison with electroneurography results showed that the motor distal latency correlated positively with the maximum MD and negatively with the minimum FA (not shown, see Fig. 5 in P4).

Figure 20 (three leftmost columns) shows the large inter-subject variation in MD (top panels) and FA (bottom panels) values along the nerve and the overlap of these values between the groups. The only consistent difference was the higher MD in the distal nerve of preoperative patients compared with control groups. Although within-subject variability along the nerve was large as well (Figure 20, rightmost column), our preliminary test-retest reliability results showed that the mean values remained stable across the scanning sessions.

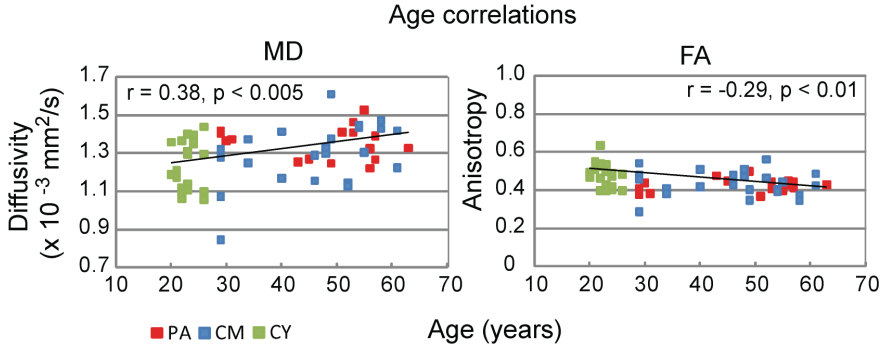

Figure 19: Positive correlations between age and MD *(left panel)*, and negative correlations between age and FA *(right panel)*. *Red squares* indicate patients, *blue squares* matched controls, and *green squares* young control subjects.

Conclusion: Diffusivity and anisotropy values of pre-operative patients and matched control subjects were similar and differed only in the distal nerve. When pre-operative patients were compared with young controls and post-operative patients, increased diffusivity and decreased anisotropy in carpal tunnel and distal median nerve were the clearest findings. Post-operative improvement was reflected in diffusivity but not in anisotropy.

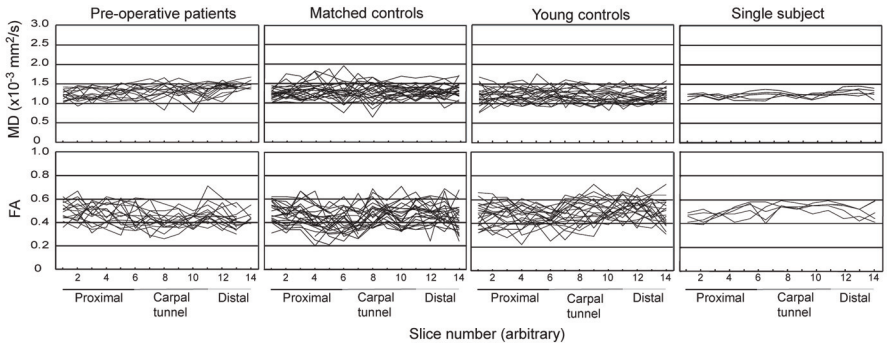

Figure 20: Slice-wise analysis of MD (*top panels*) and FA (*bottom panels*) in pre-operative patients, matched controls, young controls, and a single subject (scanned five times). Values are shown as a function of slice location from proximal to distal nerve indicated as lines below the graphs.

5 General discussion

This thesis was produced at the time when DTI was introduced in our laboratory. The first two methodological publications, P1 and P2, focused on the technical challenges resulting from DTI-related mechanical vibrations and pre-processing-effects on DTI–VBA. Publications P3 and P4 presented a novel application of DTI on distal peripheral nerves, and further utilized DTI to study patients with an entrapment of the median nerve in the upper limb.

Vibration-related movements, their effect, and correction (P1)

DTI recordings are very sensitive to any motion within the imaging area, and therefore are easily disturbed by *e.g.* subject movement, physiological motion, or mechanical vibration of the MRI system. P1 showed that vibrations differ in strength and phase within the MRI scanner and surroundings. The vibration levels clearly increased with higher b-values, usage of ECC, multiple diffusion-sensitizing gradient directions, and with a subject on the patient table. The vibration originated from gradient coils, and was remarkably enhanced by online ECC, probably due to the low-frequency switching rate of diffusion-sensitizing gradients that happened to be near the scanner's specific mechanical resonance frequency. The largest movements occurred during the readout period, thus affecting the accuracy of diffusion measurements as well as image quality. We focused on quantification of vibrations without inspecting the actual images, as no clear effects were visible in the brain images, and we did not have a proper fiber phantom for further studies. Later Gallichan and coworkers (2010) studied the effect of vibrations on image quality and found a strong, localized signal loss in the mesial parietal lobe when a diffusion gradient was applied in the right–left-direction; this signal loss appeared as high anisotropy in the FA map and as an erroneous tract in right–left direction in DEC map and tractography.

The effect of vibrations: Vibrations can cause blurring, ghosting, and general inaccuracies in diffusion quantification; the effect depends on when the vibration-related movement occurs during the sequence. Movement during the readout period and data sampling can cause spatial translation of spins and thereby

result in motional blurring and loss of spatial accuracy in the images (Wedeen et al. 1989). Moreover, motion between phase-encoding steps can modulate the amplitude or the phase MRI signal and manifests as ghosting artefacts in the phase-encoding direction (Axel et al. 1986). Movement between excitation and readout can cause similar signal losses as diffusion of water molecules, as was shown by Gallichan and coworkers (2010). However, if the movement is coherent in nature, such as blood flow in major vessels, it produces a shift of signal phase that is invisible in MR images when only magnitude information is used for image formation. In practice, however, as motion patterns are typically complex, they may bias the quantification of diffusion towards artificially increased diffusivity.

How vibrations can be decreased: Turning off ECC and adjusting the b-value ($b \leq 1000$ s/mm^2) were the easiest ways to reduce the vibrations in our scanner. More challenging approaches include redesigning the timings and gradient waveforms of the DTI sequence to avoid the scanner's mechanical resonances, redesigning patient bed, or repositioning the gradient coils in the vacuum. The latter two modifications are, however, difficult to accomplish by the user.

Gallichan and coworkers (2010) applied k-space parallel accelerated imaging instead of partial Fourier imaging (with 3/4 coverage) to avoid vibration-related artifact in their scanner.

DTI–VBA (P2)

In contrast to our preliminary assumption for lesion detection at signal intensity increase/decrease of 5–20%, far greater intensity increase/decreases were required, depending on lesion extent. The detection thresholds were high for MD and FA images with spatial normalization and smoothing in the presence of inter-individual variation. Generally, to detect a 30% MD increase robustly, lesions larger than 100 voxels were required, and 200 voxels were required for FA decrease. Therefore, conventional DTI–VBA does not outperform the visual inspection of images performed by an expert radiologist.

The main likely reasons for high detection thresholds were the coregistration inaccuracies during spatial normalization and isotropic smoothing. Therefore, currently available methodological improvements in the analysis chain, such as registration methods that better account for the special nature of diffusion tensor data (see Section “Recent methodological improvements of VBA”), should be applied in the analysis. A comparison study (Zhang et al. 2007) showed that the performance of such high dimensional spatial normalization method was superior

compared with ordinary SPM2 normalization, and in practice, white matter differences in patients *vs.* control subjects comparisons were detected better.

According to matched filter theory, the optimal smoothing kernel would be the same size as the lesion, but only when background in homogeneous. In DTI, this requirement does not fulfill (Lee et al. 2007). During isotropic smoothing, smoothed voxel values are calculated as a weighted average of current and adjacent voxel values; the FWHM of the filter defines how distant voxels contribute to the current voxel value. Therefore, the properties of surrounding tissues affect the smoothed values. For example, gray matter has low, and white matter moderate-to-high FA, whereas the MD is approximately equal in both tissues. The near-zero FA and high MD in CSF can also confuse the analysis in the brain areas nearby. Partially for this reason, the results in different brain areas were different. Another contributing factor to differences in results between the brain areas was likely partial volume effect during the scanning. If only isotropic filtering is applied, the results should also be inspected without filtering.

DTI of distal peripheral nerves (P3 and P4)

Our feasibility study (P3) from 2005 on healthy subjects showed that human distal nerves in upper and lower limbs can be imaged by means of DTI, quantified with ADC (or MD) and FA, and that the course of nerves in 3D can be visualized with tractography. More recently, several publications have utilized DTI on peripheral nerves, resulting in methodological developments and novel clinical applications (Khalil et al. 2008, Stein et al. 2009, Vargas et al. 2010, Chhabra et al. 2012, Karampinos et al. 2012, Tanitame et al. 2012, Van der Jagt et al. 2012). For example, Karampinos and coworkers (2012) were able to record good-quality DTI data from lumbar nerve roots using a novel reduced-FOV SS-SE-EPI acquisition that minimized partial volume effects, breathing artifacts, and geometric distortions.

Group comparisons: As a continuation of P3, we applied pre- and post-operative DTI recordings on the median nerve in patients with carpal tunnel syndrome, and on two control groups (age- and gender matched, and young control group) in P4. Our group comparisons revealed similar diffusivity levels in pre-operative patients and matched controls, and in post-operative patients and young controls. The only clear CTS-related difference was increased diffusivity in the distal nerve in pre-operative patients. However, their MD and parallel diffusivity values returned to the normal level of young controls post-operatively. The

similarity between pre-operative patients and matched controls indicates that age and hand strain may cause similar diffusivity changes as those produced by CTS. Our results are well in line with similar reports showing equal diffusivities in patients and elder age-matched controls (Khalil et al. 2008, Guggenberger et al. 2012b, Tasdelen et al. 2012).

Higher perpendicular diffusion in our post-operative patients than in control groups probably reflected loose space, greater isotropic diffusion or incomplete recovery of the nerve; this view was supported by similar FA in pre- and post-operative patients. Young controls had the highest FA due to tight and compact nerve structures. Lowest FA in post-operative patients combined with lowered MD may also be due to gliosis or surgery-related tissue changes.

In contrast to our findings, some studies in CTS patients *vs.* age-matched controls demonstrated only lowered FA values or lowered FA and increased MD values in carpal tunnel area (Khalil et al. 2008, Tasdelen et al. 2012, Wang et al. 2012). Moreover, in-line with our results, comparison between patients and young control subjects revealed lower FA values and higher ADC values in the carpal tunnel of patients (Stein et al. 2009, Guggenberger et al. 2012b).

Effect of age and correlations: The effect of age was clearly visible in FA and MD values and was also revealed by correlation analysis that showed decreased FA and increased MD with advancing age, in line with other recent studies of median nerve (Guggenberger et al. 2012b, Tanitame et al. 2012).

We found significant correlation only between motor distal latency and maximum MD/minimum FA. However, Wang and coworkers (2012) have reported correlations between DTI (ADC, FA) and motor conduction velocity, sensory conduction velocity, and motor distal latency. Our results showed mild correlations with conduction velocities as well but did not reach statistical significance, probably because our patient group contained mostly patients with mild and moderate CTS.

Variation in MD and FA values: MD and FA values varied considerably along the nerve within subjects, between subjects, and between scanning sessions of the same subject. Similar, rather large variations in these values was recently demonstrated along healthy median and ulnar nerves (Zhou et al. 2012). Moreover, comparisons of our absolute MD and FA values with those presented in other studies showed large between-laboratory variations, similarly to findings reported in multicenter brain studies (Zhu et al. 2011), with the best consistency within young subjects.

Since our MD and FA values between patient and control subjects partially overlapped, we were unable to define any thresholds for pathological findings.

However, Guggenberger and coworkers (2012b), who had larger between-groups differences with less overlap, suggested thresholds for pathological MD and FA values in CTS. Currently, it is unclear how generalizable these thresholds are, so probably laboratories need to record their own reference values. Moreover, large variations in these values may hamper the usage of healthy subjects. In this case, a patient's intact hand (if it exists) could possibly serve as a control. Moreover, on the basis of our results, the MD and FA in the proximal part of the nerve were stable.

Methodological issues

The discrepancies in MD and FA between different studies (see above) are probably due to several factors including different MRI scanners, coils, imaging parameters and analysis methods, as well as differences in subjects (age) and patients (CTS degree). Although optimal parameters (b = 1000 s/mm^2 at 1.5 T; b = 1200 s/mm^2, FA > 0.2 and angle < 10 degrees at 3 T) for median nerve have recently been suggested (Andreisek et al. 2009, Guggenberger et al. 2012a), many methodological issues may affect the results.

The cross-sectional area of a healthy median nerve is approximately 10 mm^2, whereas our in-plane voxel size is about 1.9 mm^2 with 3 mm slice thickness (P4). Therefore, the current imaging resolution causes partial-volume effects that lower the MD and FA. Using maximum (instead of mean) values would probably better describe the actual FA values within the nerve, as we proposed in P3. Moreover, track-density imaging, a recently proposed interpolation method in brain imaging (Calamante et al. 2010), could also improve the tracking of peripheral nerves. The basic idea is to interpolate the image to a better resolution than the original recorded image by dividing each voxel into subvoxels. During tracking, long-range information of fiber tracts is utilized so that besides the fiber information in the present voxel, also the direction and density of fibers in the neighboring voxels is used. If neighbor voxels show consistent and dense tracts that seem to pass through a subvoxel with low FA due to partial volume effect, the tract can be interpolated through the subvoxel.

Eddy current artifacts cause blurring of images and inaccuracies in diffusion recordings; their corrections result in improved registration of images. We did not utilize eddy current correction (ECC) in our median nerve recordings, as artifacts seemed not to influence greatly the position and course of the nerve, as verified by the coregistered T1-weighted image. We also checked the quality and approximate

registration of diffusion-weighted images recorded with different gradient directions by visual inspection. In future recordings, however, we most likely will apply ECC during preprocessing, after defining its impact on FA and MD values.

Generally, to avoid most of the technical pitfalls, quality assurance measurements, specifically designed for DTI, should be carried out regularly, and proper pilot studies should be done before actual subjects are scanned.

Our studies evidently suffered from small sample sizes (N = 10 in P2, N = 12 + 12 + 12 in P4), similarly to most of the DTI studies (N = 2–13 patients) on peripheral nerves until recent a study of 38 patients (Tasdelen et al. 2012). In addition, we lacked patients with severe CTS, as patients are typically operated before severe condition arises to avoid permanent axon damage. If we had more patients with severe CTS, we might have had larger differences in the group comparisons of patients *vs*. age-matched controls. Generally, much larger patient populations are required to reveal the relationships between CTS degree, DTI findings, and underlying disease dynamics and etiology.

Recent studies on peripheral nerves show good image quality despite challenges due to artifacts and CSF. Improved image quality is most likely due to multichannel coils, parallel imaging, and sequence development, which we were unfortunately unable to utilize. Parallel imaging effectively reduces the artifacts by allowing smaller echo times. Moreover, in the future, high-resolution DTI and higher field strengths (*e.g.* 7 T) may further improve image quality.

DTI studies on peripheral nerves emerge

Our methodological DTI study on distal peripheral nerves may have triggered a completely novel research area. Concurrently with our CTS study, several other DTI studies on peripheral nerves were published; some of them on CTS. DTI of peripheral nerves thus seems to have become popular. Novel applications on brachial plexus, sacral plexus and lumbar nerve roots are promising in clinical usage to demonstrate tract displacement, deformations, infiltrations, and disruption, thereby providing additional information to the current anatomic MR images and electrophysiological recordings (Vargas et al. 2010, Karampinos et al. 2012, Van der Jagt et al. 2012). Despite obvious challenges in the selection of reference values, and intra-subject, inter-subject and between-laboratory variations in MD and FA values, DTI is a promising tool for the diagnostics and follow-up of different pathologies, trauma, and entrapments, providing new insights to imaging of peripheral nerves.

In clinical applications, it would be advantageous to combine DTI with electrophysiological recordings, MRI neurography, and ultrasound. Moreover, other quantitative MRI methods, such as T2 relaxometry and magnetic transfer ratio, could provide useful information for the systematic methodological evaluation of these methods, as was recently proposed (Gambarota et al. 2012, Karampinos et al. 2012).

Acknowledgements

This work was carried out in the Brain Research Unit (BRU) of the O.V. Lounasmaa Laboratory, and Advanced Magnetic Imaging (AMI) Centre (currently part of Aalto NeuroImaging), Aalto University School of Science. Financial support from the Academy of Finland (National Center of Excellence Program 2006–2011), the EVO of Helsinki and Uusimaa Hospital District, Instrumentarium Foundation, Louis-Jeantet Foundation (Switzerland), Jenny and Antti Wihuri Foundation, and aivoAALTO research project of Aalto University was essential for different parts of the thesis.

I express my deepest gratitude to my supervisor, Acad. Professor Riitta Hari, the director of BRU, for her guidance, flexibility, and encouraging attitude, and for giving me enough freedom to think, plan, and carry out the studies. I am thankful to all my coauthors, to Sakari Arvela, Harry Göransson, Riitta Hari, Raimo Joensuu, Veikko Jousmäki, Erika Kirveskari, Nina Lindfors, Kiti Müller, Jussi Numminen, Raimo Sepponen, Mika Seppä, and Taru Suortti, for good collaboration and discussions. I specially thank Erika Kirveskari for her enthusiasm for clinical applications of DTI, for her neurophysiological expertise, positive attitude, and good company. Marita Kattelus has been invaluable help in MRI recordings, searching for journal articles, testing the MRI sequences and imaging parameters, and in many more practicalities. Thank you, Marita, for your precise work, and especially for many nice discussions and laughs. I thank Nuutti Vartiainen for help in recordings and clinical examinations.

I thankfully acknowledge the pre-reviewers Prof. Andrew Alexander and Prof. Hannu Eskola for their insightful comments and suggestions, Dr. Raimo Joensuu for reading the thesis manuscript, and Dr. Cathy Nangini for the language corrections.

I thank the former and current laboratory directors, Profs. Mikko Paalanen and Pertti Hakonen as well as all senior scientists in BRU for excellent working facilities, infrastructure, and a top-class scientific atmosphere. I am grateful to Teija Halme, Olga Jakkola, Susanna Jauhiainen, Mari Kaarni, Pirjo Muukkonen, Liisi Pasanen, Kirsi Romanoff, and Katariina Toivonen for administration and for all the practicalities you have taken care for me. I thank Jan Kujala, Petteri Räisänen, and Ronny Schreiber for computer and software support. I thank Dr. Martti Soiva for support and nice discussions.

I thank my AMI roommies Jaakko Hotta, Miika Koskinen, Veli-Matti Saarinen, and Mika Seppä, for the nice office atmosphere and interesting

discussions (plus super-nice ice-cubes!). I remain beholden to all my brave test subjects, mainly from our laboratory, who volunteered for pilot recordings and optimization of imaging parameters.

I gratefully acknowledge the DTI sequence and recon code from Drs. Roland Bammer, Michael Moseley, and Gary Glover, supported by the NIH NCCR grant "Stanford Center for Advanced Magnetic Resonance Technology", P41 RR009784 (PI: G. Glover). I thank Franck Girard, Scott Hinks, Kikka Lilius, Jorma Linnanmäki, Eero Mykrä, Harri Pättikangas, and Markus Salonen from GE Healthcare for technical support, and the VTT Technical Research Centre of Finland for the interferometer.

Special thanks go to friends, colleagues, relatives and family members, Irina Forsman, Susanna Haatainen, Anna-Liisa Hiltunen, Hanna Perkola, Maria Perkola and Dean Elliott, Paula Perkola and Toby Murray, Tuomas Perkola and Riikka-Maria Jämsén, Kati Pettersson, Kati Renvall, and Jussi Virkkala. Without you, life would be much more serious.

I express my warmest thanks to my spouse Markku and our sweet little (big!) daughter Ada. Thank you, Markku, for your patience, encouragement, insightful comments on scientific issues, good beefs, and good sense of humour even in the darkest days. Ada, our sunshine, thanks for smiles, hugs, debates and for reminding me that thesis is paper and you are more important.

Espoo, May 2013 Jaana Hiltunen

Bibliography

Alexander DC, Pierpaoli C, Basser PJ, and Gee JC: Spatial transformations of diffusion tensor magnetic resonance images. IEEE Trans Med Imaging 2001, 20(11): 1131–1139.

Anderson AW, and Ding Z: Sub-voxel measurement of fiber orientation using high angular resolution diffusion tensor imaging. Proceedings of the 10th Annual Meeting of the ISMRM, Honolulu, 2002.

Andreisek G, White LM, Kassner A, Tomlinson G, and Sussman MS: Diffusion tensor imaging and fiber tractography of the median nerve at 1.5T: optimization of b value. Skeletal Radiol 2009, 38(1): 51–59.

Assaf Y, and Cohen Y: Non-mono-exponential attenuation of water and N-acetyl aspartate signals due to diffusion in brain tissue. J Magn Reson 1998, 131(1): 69–85.

Assaf Y, and Basser PJ: Composite hindered and restricted model of diffusion (CHARMED) MR imaging of the human brain. Neuroimage 2005, 27(1): 48–58.

Axel L, Summers RM, Kressel HY, and Charles C: Respiratory effects in two-dimensional Fourier transform MR imaging. Radiol 1986, 160(3): 795–801.

Basser PJ, Mattiello J, and LeBihan D: Estimation of the effective self-diffusion tensor from the NMR spin echo. J Magn Reson B 1994a, 103(3): 247–254.

Basser PJ, Mattiello J, and LeBihan D: MR diffusion tensor spectroscopy and imaging. Biophys J 1994b, 66(1): 259–267.

Basser PJ, and Pierpaoli C: Microstructural and physiological features of tissues elucidated by quantitative-diffusion-tensor MRI. J Magn Reson B 1996, 111(3): 209–219.

Basser PJ, Pajevic S, Pierpaoli C, Duda J, and Aldroubi A: In vivo fiber tractography using DT-MRI data. Magn Reson Med 2000, 44(4): 625–632.

Beaulieu C: The basis of anisotropic water diffusion in the nervous system - a technical review. NMR Biomed 2002, 15(7-8): 435–455.

Beaulieu C: The biological basis of diffusion anisotropy. In: Diffusion MRI: From Quantitative Measurement to in Vivo Neuroanatomy. Johansen-Berg H and Behrens T E J (Eds.), Elsevier Inc., 2009, pp. 105–126.

Behrens TE, Woolrich MW, Jenkinson M, Johansen-Berg H, Nunes RG, Clare S, Matthews PM, Brady JM, and Smith SM: Characterization and propagation of uncertainty in diffusion-weighted MR imaging. Magn Reson Med 2003, 50(5): 1077–1088.

Behrens TE, Berg HJ, Jbabdi S, Rushworth MF, and Woolrich MW: Probabilistic diffusion tractography with multiple fibre orientations: What can we gain? Neuroimage 2007, 34(1): 144–155.

Bernstein MA, King KF, and Xiaohong JZ: Handbook of MRI Pulse Sequences. Elsevier Academic Press, 2004.

Bodini B, and Ciccarelli O: Diffusion MRI in neurological disorders. In: Diffusion MRI: From Quantitative Measurement to in Vivo Neuroanatomy. Johansen-Berg H and Behrens T E J (Eds.), Elsevier Inc., 2009, pp. 175–203.

Borroni B, Brambati SM, Agosti C, Gipponi S, Bellelli G, Gasparotti R, Garibotto V, Di Luca M, Scifo P, Perani D, and Padovani A: Evidence of white matter changes on diffusion tensor imaging in frontotemporal dementia. Arch Neurol 2007, 64(2): 246–251.

Calamante F, Tournier J-D, Jackson GD, and Connelly A: Track-density imaging (TDI): Super-resolution white matter imaging using whole-brain track-density mapping. Neuroimage 2012, 53: 1233–1243.

Cartwright MS, Hobson-Webb LD, Boon AJ, Alter KE, Hunt CH, Flores VH, Werner RA, Shook SJ, Thomas TD, Primack SJ, and Walker FO: Evidence-based guideline: neuromuscular ultrasound for the diagnosis of carpal tunnel syndrome. Muscle Nerve 2012, 46(2): 287–293.

Catani M, Howard RJ, Pajevic S, and Jones DK: Virtual in vivo interactive dissection of white matter fasciculi in the human brain. Neuroimage 2002, 17(1): 77–94.

Chhabra A, Thakkar RS, Andreisek G, Chalian M, Belzberg AJ, Blakeley J, Hoke A, Thawait GK, Eng J, and Carrino JA: Anatomic MR imaging and functional diffusion tensor Imaging of peripheral nerve tumors and tumorlike conditions. Am J Neuroradiol 2013, 34(4): 802–807.

Clark CA, and Werring DJ: Diffusion tensor imaging in spinal cord: methods and applications - a review. NMR Biomed 2002, 15(7-8): 578–586.

Conturo TE, McKinstry RC, Akbudak E, and Robinson BH: Encoding of anisotropic diffusion with tetrahedral gradients: a general mathematical diffusion formalism and experimental results. Magn Reson Med 1996, 35(3): 399–412.

Conturo TE, Lori NF, Cull TS, Akbudak E, Snyder AZ, Shimony JS, McKinstry RC, Burton H, and Raichle ME: Tracking neuronal fiber pathways in the living human brain. Proc Natl Acad Sci U S A 1999, 96(18): 10422–10427.

Cooper RL, Chang DB, Young AC, Martin CJ, and Ancker-Johnson D: Restricted diffusion in biophysical systems. Experiment. Biophys J 1974, 14(3): 161–177.

Cudlip SA, Howe FA, Clifton A, Schwartz MS, and Bell BA: Magnetic resonance neurography studies of the median nerve before and after carpal tunnel decompression. J Neurosurg 2002, 96(6): 1046–1051.

Descoteaux M, Deriche R, Knösche TR, and Anwander A: Deterministic and probabilistic tractography based on complex fibre orientation distributions. IEEE Trans Med Imaging 2009, 28:269–286.

Dou J, Reese TG, Tseng WY, and Wedeen VJ: Cardiac diffusion MRI without motion effects. Magn Reson Med 2002, 48(1): 105–114.

Engelbrecht V, Scherer A, Rassek M, Witsack HJ, and Modder U: Diffusion-weighted MR imaging in the brain in children: findings in the normal brain and in the brain with white matter diseases. Radiol 2002, 222(2): 410–418.

Filler AG, Howe FA, Hayes CE, Kliot M, Winn HR, Bell BA, Griffiths JR, and Tsuruda JS: Magnetic resonance neurography. Lancet 1993, 341(8846): 659–661.

Filler AG, Kliot M, Howe FA, Hayes CE, Saunders DE, Goodkin R, Bell BA, Winn HR, Griffiths JR, and Tsuruda JS: Application of magnetic resonance neurography in the evaluation of patients with peripheral nerve pathology. J Neurosurg 1996, 85(2): 299–309.

Frank LR: Anisotropy in high angular resolution diffusion-weighted MRI. Magn Reson Med 2001, 45(6): 935–939.

Gallichan D, Scholz J, Bartsch A, Behrens TE, Robson MD, and Miller KL: Addressing a systematic vibration artifact in diffusion-weighted MRI. Hum Brain Mapp 2010, 31(2): 193–202.

Gambarota G, Krueger G, Theumann N, and Mekle R: Magnetic resonance imaging of peripheral nerves: differences in magnetization transfer. Muscle Nerve 2012, 45(1): 13–17.

Gideon P, Thomsen C, and Henriksen O: Increased self-diffusion of brain water in normal aging. J Magn Reson Imaging 1994, 4(2): 185–188.

Goodlett C, Davis B, Jean R, Gilmore J, and Gerig G: Improved correspondence for DTI population studies via unbiased atlas building. Med Image Comput Comput Assist Interv 2006, 9(Pt 2): 260–267.

Grant GA, Britz GW, Goodkin R, Jarvik JG, Maravilla K, and Kliot M: The utility of magnetic resonance imaging in evaluating peripheral nerve disorders. Muscle Nerve 2002, 25(3): 314–331.

Grant GA, Goodkin R, Maravilla KR, and Kliot M: MR neurography: diagnostic utility in the surgical treatment of peripheral nerve disorders. Neuroimaging Clin N Am 2004, 14(1): 115–133.

Guggenberger R, Eppenberger P, Markovic D, Nanz D, Chhabra A, Pruessmann KP, and Andreisek G: MR neurography of the median nerve at 3.0T: optimization of diffusion tensor imaging and fiber tractography. Eur J Radiol 2012a, 81(7): 775–782.

Guggenberger R, Markovic D, Eppenberger P, Chhabra A, Schiller A, Nanz D, Prussmann K, and Andreisek G: Assessment of median nerve with MR

neurography by using diffusion-tensor imaging: normative and pathologic diffusion values. Radiology 2012b, 265(1): 194–203.

Guimond A, Meunier J, and Thirion JP: Average brain models: A convergence study. Computer Vision Image Understand 2000, 77: 192–210.

Hansen JR: Pulsed NMR study of water mobility in muscle and brain tissue. Biochim Biophys Acta 1971, 230(3): 482–486.

Hasan KM, Parker DL, and Alexander AL: Comparison of gradient encoding schemes for diffusion-tensor MRI. J Magn Reson Imaging 2001, 13(5): 769–780.

Hermoye L, Saint-Martin C, Cosnard G, Lee SK, Kim J, Nassogne MC, Menten R, Clapuyt P, Donohue PK, Hua K, Wakana S, Jiang H, van Zijl PC, and Mori S: Pediatric diffusion tensor imaging: normal database and observation of the white matter maturation in early childhood. Neuroimage 2006, 29(2): 493–504.

Hiltunen J, Seppa M, and Hari R: Diffuusiotensorikuvaus hermoratojen tutkimuksessa. Duodecim 2007, 123(15): 1851–1858.

Horsfield MA, and Jones DK: Applications of diffusion-weighted and diffusion tensor MRI to white matter diseases - a review. NMR Biomed 2002, 15(7-8): 570–577.

Huppi PS, Maier SE, Peled S, Zientara GP, Barnes PD, Jolesz FA, and Volpe JJ: Microstructural development of human newborn cerebral white matter assessed in vivo by diffusion tensor magnetic resonance imaging. Pediatr Res 1998, 44(4): 584–590.

Jansons KM, and Alexander DC: Persistent Angular Structure: new insights from diffusion MRI data. Dummy version. Inf Process Med Imaging 2003, 18: 672–683.

Jarvik JG, Kliot M, and Maravilla KR: MR nerve imaging of the wrist and hand. Hand Clin 2000, 16(1): 13–24.

Jarvik JG, and Yuen E: Diagnosis of carpal tunnel syndrome: electrodiagnostic and magnetic resonance imaging evaluation. Neurosurg Clin N Am 2001, 12(2): 241–253.

Jarvik JG, Yuen E, Haynor DR, Bradley CM, Fulton-Kehoe D, Smith-Weller T, Wu R, Kliot M, Kraft G, Wang L, Erlich V, Heagerty PJ, and Franklin GM: MR nerve imaging in a prospective cohort of patients with suspected carpal tunnel syndrome. Neurology 2002, 58(11): 1597–1602.

Jarvik JG, Yuen E, and Kliot M: Diagnosis of carpal tunnel syndrome: electrodiagnostic and MR imaging evaluation. Neuroimaging Clin N Am 2004, 14(1): 93–102.

Jbabdi S, Woolrich MW, Andersson JL, and Behrens TE: A Bayesian framework for global tractography. Neuroimage 2007, 37(1): 116–129.

Jensen JH, Helpern JA, Ramani A, Lu H, and Kaczynski K: Diffusional kurtosis imaging: the quantification of non-Gaussian water diffusion by means of magnetic resonance imaging. Magn Reson Med 2005, 53(6): 1432–1440.

Jiang H, van Zijl PC, Kim J, Pearlson GD, and Mori S: DtiStudio: resource program for diffusion tensor computation and fiber bundle tracking. Comput Methods Programs Biomed 2006, 81(2): 106–116.

Johansen-Berg H, and Behrens TE (Eds.): Diffusion MRI: From Quantitative Measurement to In Vivo Neuroanatomy, Academic Press, 2009.

Jones DK, Horsfield MA, and Simmons A: Optimal strategies for measuring diffusion in anisotropic systems by magnetic resonance imaging. Magn Reson Med 1999a, 42(3): 515–525.

Jones DK, Simmons A, Williams SC, and Horsfield MA: Non-invasive assessment of axonal fiber connectivity in the human brain via diffusion tensor MRI. Magn Reson Med 1999b, 42(1): 37–41.

Jones DK, Griffin LD, Alexander DC, Catani M, Horsfield MA, Howard R, and Williams SC: Spatial Normalization and Averaging of Diffusion Tensor MRI Data Sets. Neuroimage 2002, 19: 592–617.

Jones DK: Determining and visualizing uncertainty in estimates of fiber orientation from diffusion tensor MRI. Magn Reson Med 2003, 49(1): 7–12.

Jones DK: The effect of gradient sampling schemes on measures derived from diffusion tensor MRI: a Monte Carlo study. Magn Reson Med 2004, 51(4): 807–815.

Jones DK, and Basser PJ: "Squashing peanuts and smashing pumpkins": how noise distorts diffusion-weighted MR data. Magn Reson Med 2004, 52: 979–993.

Jones DK, Symms MR, Cercignani M, and Howard RJ: The effect of filter size on VBM analyses of DT-MRI data. Neuroimage 2005, 26(2): 546–554.

Jones DK, and Cercignani M: Twenty-five pitfalls in the analysis of diffusion MRI data. NMR in Biomed 2010, 23: 803–820.

Jones DK (Ed.): Diffusion MRI: Theory, Methods, and Applications Oxford University Press, 2011.

Jones DK, Knösche TR, and Turner R: White matter integrity, fiber count, and other fallacies: The do's and don'ts of diffusion MRI. Neuroimage 2013, 73: 239–254.

Kabakci N, Gurses B, Firat Z, Bayram A, Ulug AM, Kovanlikaya A, and Kovanlikaya I: Diffusion tensor imaging and tractography of median nerve: normative diffusion values. Am J Roentgenol 2007, 189(4): 923–927.

Kabakci NT, Kovanlikaya A, and Kovanlikaya I: Tractography of the median nerve. Semin Musculoskelet Radiol 2009, 13(1): 18–23.

Karampinos DC, Melkus G, Shepherd TM, Banerjee S, Saritas EU, Shankaranarayanan A, Hess CP, Link TM, Dillon WP, and Majumdar S:

Diffusion tensor imaging and T2 relaxometry of bilateral lumbar nerve roots: feasibility of in-plane imaging. NMR Biomed 2013, 26(6): 630–637.

Khalil C, Hancart C, Le Thuc V, Chantelot C, Chechin D, and Cotten A: Diffusion tensor imaging and tractography of the median nerve in carpal tunnel syndrome: preliminary results. Eur Radiol 2008, 18(10): 2283–2291.

Koay CG: Least squares approaches to diffusion tensor imaging. In: Diffusion Tensor: Theory, Methods, and Applications. Jones D K (Ed.), Oxford University Press, 2011, pp. 272–284.

Koch MA, Norris DG, and Hund-Georgiadis M: An investigation of functional and anatomical connectivity using magnetic resonance imaging. Neuroimage 2002, 16(1): 241–250.

Kreher BW, Mader I, and Kiselev VG: Gibbs tracking: a novel approach for the reconstruction of neuronal pathways. Magn Reson Med 2008, 60(4): 953–963.

Lazar M, Weinstein DM, Tsuruda JS, Hasan KM, Arfanakis K, Meyerand ME, Badie B, Rowley HA, Haughton V, Field A, and Alexander AL: White matter tractography using diffusion tensor deflection. Hum Brain Mapp 2003, 18(4): 306–321.

Le Bihan D, Breton E, Lallemand D, Grenier P, Cabanis E, and Laval-Jeantet M: MR imaging of intravoxel incoherent motions: application to diffusion and perfusion in neurologic disorders. Radiology 1986, 161(2): 401–407.

Le Bihan D, Delannoy J, and Levin RL: Temperature mapping with MR imaging of molecular diffusion: application to hyperthermia. Radiology 1989, 171(3): 853–857.

Le Bihan D: Molecular diffusion nuclear magnetic resonance imaging. Magn Reson Q 1991, 7(1): 1–30.

Le Bihan D: Molecular diffusion, tissue microdynamics and microstructure. NMR Biomed 1995, 8(7-8): 375–386.

Le Bihan D, Mangin JF, Poupon C, Clark CA, Pappata S, Molko N, and Chabriat H: Diffusion tensor imaging: concepts and applications. J Magn Reson Imaging 2001, 13(4): 534–546.

Le Bihan D: Looking into the functional architecture of the brain with diffusion MRI. Nat Rev Neurosci 2003, 4(6): 469–480.

Lee JE, Chung MK, Lazar M, DuBray MB, Kim J, Bigler ED, Lainhart JE, and Alexander AL: A study of diffusion tensor imaging by tissue-specific smoothing-compensated voxel-based analysis. Neuroimage 2009, 44(3): 870–883.

Leemans A, and Jones DK: The B-matrix must be rotated when correcting for subject motion in DTI data. Magn Reson Med 2009, 61(6): 1336–1349.

Liang Z-P, and Lauterburg PC: Principles of Magnetic Resonance Imaging. New York, IEEE Press, 2000.

McRobbie DW, Moore EA, Graves MJ, and Prince MR: MRI From Picture to Proton, Second Edition. Cambridge University Press, 2007.

Meek MF, Stenekes MW, Hoogduin HM, and Nicolai JP: In vivo three-dimensional reconstruction of human median nerves by diffusion tensor imaging. Exp Neurol 2006, 198(2): 479–482.

Mhoon JT, Juel VC, and Hobson-Webb LD: Median nerve ultrasound as a screening tool in carpal tunnel syndrome: Correlation of cross-sectional area measures with electrodiagnostic abnormality. Muscle Nerve 2012, 46(6): 861–870.

Monagle K, Dai G, Chu A, Burnham RS, and Snyder RE: Quantitative MR imaging of carpal tunnel syndrome. Am J Roentgenol 1999, 172(6): 1581–1586.

Mori S, Crain BJ, Chacko VP, and van Zijl PC: Three-dimensional tracking of axonal projections in the brain by magnetic resonance imaging. Ann Neurol 1999, 45(2): 265–269.

Mori S, Frederiksen K, Van Zijl PCM, Stieltjes B, Kraut MA, Solaiyappan M, and Pomper MG: Brain white matter anatomy of tumor patients evaluated with diffusion tensor imaging. Ann Neurol 2002a, 51: 377–380.

Mori S, Kaufmann WE, Davatzikos C, Stieltjes B, Amodei L, Fredericksen K, Pearlson GD, Melhem ER, Solaiyappan M, Raymond GV, Moser HW, and van Zijl PC: Imaging cortical association tracts in the human brain using diffusion-tensor-based axonal tracking. Magn Reson Med 2002b, 47(2): 215–223.

Mori S, Wakana S, Nagae-Poetscher L, and Van Zijl P: MRI Atlas of Human White Matter. Elsevier, 2005.

Mori S: Introduction to Diffusion Tensor Imaging. Elsevier, 2007.

Mori S, Oishi K, Jiang H, Jiang L, Li X, Akhter K, Hua K, Faria AV, Mahmood A, Woods R, Toga AW, Pike GB, Neto PR, Evans A, Zhang J, Huang H, Miller MI, van Zijl P, and Mazziotta J: Stereotaxic white matter atlas based on diffusion tensor imaging in an ICBM template. Neuroimage 2008, 40(2): 570–582.

Moseley ME, Cohen Y, Kucharczyk J, Mintorovitch J, Asgari HS, Wendland MF, Tsuruda J, and Norman D: Diffusion-weighted MR imaging of anisotropic water diffusion in cat central nervous system. Radiology 1990, 176(2): 439–445.

Moseley ME, Kucharczyk J, Asgari HS, and Norman D: Anisotropy in diffusion-weighted MRI. Magn Reson Med 1991, 19(2): 321–326.

Moseley ME, Butts K, Yenari MA, Marks M, and de Crespigny A: Clinical aspects of DWI. NMR Biomed 1995, 8(7-8): 387–396.

Mukherjee P, Miller JH, Shimony JS, Conturo TE, Lee BC, Almli CR, and McKinstry RC: Normal brain maturation during childhood: developmental

trends characterized with diffusion-tensor MR imaging. Radiology 2001, 221(2): 349–358.

Neeman M, Freyer JP, and Sillerud LO: A simple method for obtaining cross-term-free images for diffusion anisotropy studies in NMR microimaging. Magn Reson Med 1991, 21(1): 138–143.

Neil JJ, Shiran SI, McKinstry RC, Schefft GL, Snyder AZ, Almli CR, Akbudak E, Aronovitz JA, Miller JP, Lee BC, and Conturo TE: Normal brain in human newborns: apparent diffusion coefficient and diffusion anisotropy measured by using diffusion tensor MR imaging. Radiology 1998, 209(1): 57–66.

Pajevic S, and Pierpaoli C: Color schemes to represent the orientation of anisotropic tissues from diffusion tensor data: application to white matter fiber tract mapping in the human brain. Magn Reson Med 1999, 42(3): 526–540.

Papadakis NG, Xing D, Huang CL, Hall LD, and Carpenter TA: A comparative study of acquisition schemes for diffusion tensor imaging using MRI. J Magn Reson 1999, 137(1): 67–82.

Papadakis NG, Murrills CD, Hall LD, Huang CL, and Adrian Carpenter T: Minimal gradient encoding for robust estimation of diffusion anisotropy. Magn Reson Imaging 2000, 18(6): 671–679.

Park HJ, Westin CF, Kubicki M, Maier SE, Niznikiewicz M, Baer A, Frumin M, Kikinis R, Jolesz FA, McCarley RW, and Shenton ME: White matter hemisphere asymmetries in healthy subjects and in schizophrenia: a diffusion tensor MRI study. Neuroimage 2004, 23(1): 213–223.

Parker GJ, Schnabel JA, Symms MR, Werring DJ, and Barker GJ: Nonlinear smoothing for reduction of systematic and random errors in diffusion tensor imaging. J Magn Reson Imaging 2000, 11(6): 702–710.

Parker GJ, Wheeler-Kingshott CA, and Barker GJ: Estimating distributed anatomical connectivity using fast marching methods and diffusion tensor imaging. IEEE Trans Med Imaging 2002, 21(5): 505–512.

Parker GJ, Haroon HA, and Wheeler-Kingshott CA: A framework for a streamline-based probabilistic index of connectivity (PICo) using a structural interpretation of MRI diffusion measurements. J Magn Reson Imaging 2003, 18(2): 242–254.

Parker GJ: Analysis of MR diffusion weighted images. Br J Radiol 2004, 77 Spec No 2: S176–185.

Parker GJ, and Alexander DC: Probabilistic anatomical connectivity derived from the microscopic persistent angular structure of cerebral tissue. Philos Trans R Soc Lond B Biol Sci 2005, 360(1457): 893–902.

Parker GJM, and Alexander DC: Probabilistic Monte Carlo based mapping of cerebral connections utilizing whole-brain crossing fibre information. Lect Notes Comput Sci 2003, 2732: 684–695.

Partridge SC, Mukherjee P, Henry RG, Miller SP, Berman JI, Jin H, Lu Y, Glenn OA, Ferriero DM, Barkovich AJ, and Vigneron DB: Diffusion tensor imaging: serial quantitation of white matter tract maturity in premature newborns. Neuroimage 2004, 22(3): 1302–1314.

Pierpaoli C, and Basser PJ: Toward a quantitative assessment of diffusion anisotropy. Magn Reson Med 1996, 36(6): 893–906.

Pierpaoli C, Barnett A, Pajevic S, Chen R, Penix LR, Virta A, and Basser P: Water diffusion changes in Wallerian degeneration and their dependence on white matter architecture. Neuroimage 2001, 13(6 Pt 1): 1174–1185.

Poupon C, Mangin J, Clark CA, Frouin V, Regis J, Le Bihan D, and Bloch I: Towards inference of human brain connectivity from MR diffusion tensor data. Med Image Anal 2001, 5(1): 1–15.

Provenzale JM, Liang L, DeLong D, and White LE: Diffusion tensor imaging assessment of brain white matter maturation during the first postnatal year. AJR Am J Roentgenol 2007, 189(2): 476–486.

Reese TG, Weisskoff RM, Smith RN, Rosen BR, Dinsmore RE, and Wedeen VJ: Imaging myocardial fiber architecture in vivo with magnetic resonance. Magn Reson Med 1995, 34(6): 786–791.

Ries M, Jones RA, Basseau F, Moonen CT, and Grenier N: Diffusion tensor MRI of the human kidney. J Magn Reson Imaging 2001, 14(1): 42–49.

Righini A, Bianchini E, Parazzini C, Gementi P, Ramenghi L, Baldoli C, Nicolini U, Mosca F, and Triulzi F: Apparent diffusion coefficient determination in normal fetal brain: a prenatal MR imaging study. Am J Neuroradiol 2003, 24(5): 799–804.

Roll SC, Evans KD, Li X, Freimer M, and Sommerich CM: Screening for carpal tunnel syndrome using sonography. J Ultrasound Med 2011, 30(12): 1657–1667.

Sage CA, Van Hecke W, Peeters R, Sijbers J, Robberecht W, Parizel P, Marchal G, Leemans A, and Sunaert S: Quantitative diffusion tensor imaging in amyotrophic lateral sclerosis: revisited. Hum Brain Mapp 2009, 30(11): 3657–3675.

Salat DH, Tuch DS, Greve DN, van der Kouwe AJ, Hevelone ND, Zaleta AK, Rosen BR, Fischl B, Corkin S, Rosas HD, and Dale AM: Age-related alterations in white matter microstructure measured by diffusion tensor imaging. Neurobiol Aging 2005a, 26(8): 1215–1227.

Salat DH, Tuch DS, Hevelone ND, Fischl B, Corkin S, Rosas HD, and Dale AM: Age-related changes in prefrontal white matter measured by diffusion tensor imaging. Ann N Y Acad Sci 2005b, 1064: 37–49.

Selim M, Fink JN, Kumar S, Caplan LR, Horkan C, Chen Y, Linfante I, and Schlaug G: Predictors of hemorrhagic transformation after intravenous recombinant tissue plasminogen activator: prognostic value of the initial

apparent diffusion coefficient and diffusion-weighted lesion volume. Stroke 2002, 33(8): 2047–2052.

Seok JH, Park HJ, Chun JW, Lee SK, Cho HS, Kwon JS, and Kim JJ: White matter abnormalities associated with auditory hallucinations in schizophrenia: a combined study of voxel-based analyses of diffusion tensor imaging and structural magnetic resonance imaging. Psychiatry Res 2007, 156(2): 93–104.

Seror P: Sonography and electrodiagnosis in carpal tunnel syndrome diagnosis, an analysis of the literature. Eur J Radiol 2008, 67(1): 146–152.

Sijbers J, den Dekker AJ, Van der Linden A, Verhoye TM, and Van Dyck D: Adaptive anisotropic noise filtering for magnitude MR data. Magn Reson Imaging 1999, 17(10): 1533–1539.

Sinha U, and Yao L: In vivo diffusion tensor imaging of human calf muscle. J Magn Reson Imaging 2002, 15(1): 87–95.

Skare S, Hedehus M, Moseley ME, and li T-Q: Condition number as a measure of noise performance of diffusion tensor data acquisition schemes with MRI. J Magn Reson 2000, 147: 340–352.

Skorpil M, Karlsson M, and Nordell A: Peripheral nerve diffusion tensor imaging. Magn Reson Imaging 2004, 22(5): 743–745.

Smith SM, Jenkinson M, Johansen-Berg H, Rueckert D, Nichols TE, Mackay CE, Watkins KE, Ciccarelli O, Cader MZ, Matthews PM, and Behrens TE: Tract-based spatial statistics: voxelwise analysis of multi-subject diffusion data. Neuroimage 2006, 31(4): 1487–1505.

Smith SM, Johansen-Berg H, Jenkinson M, Rueckert D, Nichols TE, Miller KL, Robson MD, Jones DK, Klein JC, Bartsch AJ, and Behrens TE: Acquisition and voxelwise analysis of multi-subject diffusion data with tract-based spatial statistics. Nat Protoc 2007, 2(3): 499–503.

Sotak CH: The role of diffusion tensor imaging in the evaluation of ischemic brain injury - a review. NMR Biomed 2002, 15(7-8): 561–569.

Stein D, Neufeld A, Pasternak O, Graif M, Patish H, Schwimmer E, Ziv E, and Assaf Y: Diffusion tensor imaging of the median nerve in healthy and carpal tunnel syndrome subjects. J Magn Reson Imaging 2009, 29(3): 657–662.

Stejskal EO, and Tanner JE: Spin diffusion measurements: spin echoes in the presence of a time-dependent field gradient. J Phys Chem 1965, 42: 288–292.

Sullivan EV, Adalsteinsson E, and Pfefferbaum A: Selective age-related degradation of anterior callosal fiber bundles quantified in vivo with fiber tracking. Cereb Cortex 2006, 16(7): 1030–1039.

Sullivan EV, Rohlfing T, and Pfefferbaum A: Quantitative fiber tracking of lateral and interhemispheric white matter systems in normal aging: relations to timed performance. Neurobiol Aging 2010, 31(3): 464–481.

Takagi T, Nakamura M, Yamada M, Hikishima K, Momoshima S, Fujiyoshi K, Shibata S, Okano HJ, Toyama Y, and Okano H: Visualization of peripheral nerve degeneration and regeneration: monitoring with diffusion tensor tractography. Neuroimage 2009, 44(3): 884–892.

Tanitame K, Iwakado Y, Akiyama Y, Ueno H, Ochi K, Otani K, Takasu M, Date S, and Awai K: Effect of age on the fractional anisotropy (FA) value of peripheral nerves and clinical significance of the age-corrected FA value for evaluating polyneuropathies. Neuroradiology 2012, 54(8): 815–821.

Tasdelen N, Gurses B, Kilickesmez O, Firat Z, Karlikaya G, Tercan M, Ulug AM, and Gurmen AN: Diffusion tensor imaging in carpal tunnel syndrome. Diagn Interv Radiol 2012, 18(1): 60–66.

Tench CR, Morgan PS, Blumhardt LD, and Constantinescu C: Improved white matter fiber tracking using stochastic labeling. Magn Reson Med 2002, 48(4): 677-683.

Tong DC, Adami A, Moseley ME, and Marks MP: Relationship between apparent diffusion coefficient and subsequent hemorrhagic transformation following acute ischemic stroke. Stroke 2000, 31(10): 2378–2384.

Toosy AT, Ciccarelli O, Parker GJ, Wheeler-Kingshott CA, Miller DH, and Thompson AJ: Characterizing function-structure relationships in the human visual system with functional MRI and diffusion tensor imaging. Neuroimage 2004, 21(4): 1452–1463.

Tournier JD, Calamante F, Gadian DG, and Connelly A: Diffusion-weighted magnetic resonance imaging fibre tracking using a front evolution algorithm. Neuroimage 2003, 20(1): 276–288.

Tournier JD, Calamante F, Gadian DG, and Connelly A: Direct estimation of the fiber orientation density function from diffusion-weighted MRI data using spherical deconvolution. Neuroimage 2004, 23(3): 1176–1185.

Tuch DS, Reese TG, Wiegell MR, and Wedeen VJ: Diffusion MRI of complex neural architecture. Neuron 2003, 40(5): 885–895.

Tuch DS: Q-ball imaging. Magn Reson Med 2004, 52(6): 1358–1372.

Van der Jagt PK, Dik P, Froeling M, Kwee TC, Nievelstein RA, ten Haken B, and Leemans A: Architectural configuration and microstructural properties of the sacral plexus: a diffusion tensor MRI and fiber tractography study. Neuroimage 2012, 62(3): 1792–1799.

Van Everdingen KJ, Van der Grond J, Kappelle LJ, Ramos LM, and Mali WP: Diffusion-weighted magnetic resonance imaging in acute stroke. Stroke 1998, 29(9): 1783–1790.

Van Hecke W, Leemans A, D'Agostino E, De Backer S, Vandervliet E, Parizel PM, and Sijbers J: Nonrigid coregistration of diffusion tensor images using a viscous fluid model and mutual information. IEEE Trans Med Imaging 2007, 26(11): 1598–1612.

Van Hecke W, Sijbers J, D'Agostino E, Maes F, De Backer S, Vandervliet E, Parizel PM, and Leemans A: On the construction of an inter-subject diffusion tensor magnetic resonance atlas of the healthy human brain. Neuroimage 2008, 43(1): 69–80.

Van Hecke W, Leemans A, De Backer S, Jeurissen B, Parizel PM, and Sijbers J: Comparing isotropic and anisotropic smoothing for voxel-based DTI analyses: A simulation study. Hum Brain Mapp 2010, 31(1): 98–114.

Vangberg TR, Skranes J, Dale AM, Martinussen M, Brubakk AM, and Haraldseth O: Changes in white matter diffusion anisotropy in adolescents born prematurely. Neuroimage 2006, 32(4): 1538–1548.

Vargas MI, Viallon M, Nguyen D, Delavelle J, and Becker M: Diffusion tensor imaging (DTI) and tractography of the brachial plexus: feasibility and initial experience in neoplastic conditions. Neuroradiology 2010, 52(3): 237–245.

Virta A, Barnett A, and Pierpaoli C: Visualizing and characterizing white matter fiber structure and architecture in the human pyramidal tract using diffusion tensor MRI. Magn Reson Imaging 1999, 17(8): 1121–1133.

Wakana S, Jiang H, Nagae-Poetscher LM, van Zijl PC, and Mori S: Fiber tract-based atlas of human white matter anatomy. Radiol 2004, 230(1): 77–87.

Wang CK, Jou IM, Huang HW, Chen PY, Tsai HM, Liu YS, and Lin CC: Carpal tunnel syndrome assessed with diffusion tensor imaging: comparison with electrophysiological studies of patients and healthy volunteers. Eur J Radiol 2012, 81(11): 3378–3383.

Wang S, Poptani H, Bilello M, Wu X, Woo JH, Elman LB, McCluskey LF, Krejza J, and Melhem ER: Diffusion tensor imaging in amyotrophic lateral sclerosis: volumetric analysis of the corticospinal tract. Am J Neuroradiol 2006, 27(6): 1234–1238.

Warach S, Dashe JF, and Edelman RR: Clinical outcome in ischemic stroke predicted by early diffusion-weighted and perfusion magnetic resonance imaging: a preliminary analysis. J Cereb Blood Flow Metab 1996, 16(1): 53–59.

Weber J, Mattle HP, Heid O, Remonda L, and Schroth G: Diffusion-weighted imaging in ischaemic stroke: a follow-up study. Neuroradiology 2000, 42(3): 184–191.

Wedeen VJ, Wendt REr, and Jerosch-Herold M: Motional phase artifacts in Fourier transform MRI. Magn Reson Med 1989, 11(1): 114–120.

Wedeen VJ, Reese TG, D.S. T, Dou J-G, Weiskoff RM, and Chessler D: Mapping fiber orientation spectra in cerebral white matter with Fourier transform

diffusion MRI. Proceedings of the 7th Annual Meeting of the ISMRM, Philadelphia, 1999.

Wedeen VJ, Reese TG, Napadow VJ, and Gilbert RJ: Demonstration of primary and secondary muscle fiber architecture of the bovine tongue by diffusion stensor magnetic resonance imaging. Biophys J 2001, 80(2): 1024–1028.

Westbrook C, Roth CK, and Talbot J: MRI in Practice. Blackwell Publishing, 2005.

Wheeler-Kingshott CA, Hickman SJ, Parker GJ, Ciccarelli O, Symms MR, Miller DH, and Barker GJ: Investigating cervical spinal cord structure using axial diffusion tensor imaging. Neuroimage 2002, 16(1): 93–102.

Xue R, van Zijl PC, Crain BJ, Solaiyappan M, and Mori S: In vivo three-dimensional reconstruction of rat brain axonal projections by diffusion tensor imaging. Magn Reson Med 1999, 42(6): 1123–1127.

Yu CS, Li KC, Xuan Y, Ji XM, and Qin W: Diffusion tensor tractography in patients with cerebral tumors: a helpful technique for neurosurgical planning and postoperative assessment. Eur J Radiol 2005, 56(2): 197–204.

Zaraiskaya T, Kumbhare D, and Noseworthy MD: Diffusion tensor imaging in evaluation of human skeletal muscle injury. J Magn Reson Imaging 2006, 24(2): 402–408.

Zhang H, Avants BB, Yushkevich PA, Woo JH, Wang S, McCluskey LF, Elman LB, and Melhem ER: High-dimensional spatial normalization of diffusion tensor images improves the detection of white matter differences: an example study using amyotrophic lateral sclerosis. IEEE Trans Med Imaging 2007, 26(11): 1585–1597.

Zhou Y, Kumaravel M, Patel VS, Sheikh KA, and Narayana PA: Diffusion tensor imaging of forearm nerves in humans. J Magn Reson Imaging 2012, 36(4): 920–927.

Zhu T, Hu R, Qiu X, Taylor M, Tso Y, Yiannoutsos C, Navia B, Mori S, Ekholm S, Schifitto G, and Zhong J: Quantification of accuracy and precision of multi-center DTI measurements: a diffusion phantom and human brain study. Neuroimage 2011, 56(3): 1398–1411.

Aalto-DD 93/2013

ISBN 978-952-60-5196-3
ISBN 978-952-60-5197-0 (pdf)
ISSN-L 1799-4934
ISSN 1799-4934
ISSN 1799-4942 (pdf)

Aalto University
School of Science
O.V. Lounasmaa Laboratory
www.aalto.fi

BUSINESS +
ECONOMY

ART +
DESIGN +
ARCHITECTURE

SCIENCE +
TECHNOLOGY

CROSSOVER

**DOCTORAL
DISSERTATIONS**